OPEN ACCESS
IOP Publishing | International Atomic Energy Agency
Nuclear Fusion
Nucl. Fusion **57** (2017) 126049 (21pp)
https://doi.org/10.1088/1741-4326/aa86fd

Performance analysis of Rogowski coils and the measurement of the total toroidal current in the ITER machine

A. Quercia[1,4], R. Albanese[1,4], R. Fresa[2,4], S. Minucci[3,4], S. Arshad[5] and G. Vayakis[6]

[1] Dipartimento di Ingegneria Elettrica e Tecnologie dell'Informazione, Università Federico II, Napoli, Italy
[2] Scuola di Ingegneria, Università della Basilicata, Potenza, Italy
[3] Dipartimento di Economia, Ingegneria, Società e Impresa, Università della Tuscia, Viterbo, Italy
[4] Consorzio CREATE, Via Claudio 21, IT-80125 Napoli, Italy
[5] Fusion for Energy (F4E), Josep Pla 2, Torres Diagonal Litoral B3, 08019 Barcelona, Spain
[6] ITER Organization, Route de Vinon-sur-Verdon, CS 90 046, 13067 St Paul Lez Durance Cedex, France

E-mail: aquercia@unina.it

Received 16 March 2017, revised 24 July 2017
Accepted for publication 18 August 2017
Published 13 October 2017

Abstract

The paper carries out a comprehensive study of the performances of Rogowski coils. It describes methodologies that were developed in order to assess the capabilities of the Continuous External Rogowski (CER), which measures the total toroidal current in the ITER machine. Even though the paper mainly considers the CER, the contents are general and relevant to any Rogowski sensor.

The CER consists of two concentric helical coils which are wound along a complex closed path. Modelling and computational activities were performed to quantify the measurement errors, taking detailed account of the ITER environment. The geometrical complexity of the sensor is accurately accounted for and the standard model which provides the classical expression to compute the flux linkage of Rogowski sensors is quantitatively validated. Then, in order to take into account the non-ideality of the winding, a generalized expression, formally analogue to the classical one, is presented. Models to determine the worst case and the statistical measurement accuracies are hence provided. The following sources of error are considered: effect of the joints, disturbances due to external sources of field (the currents flowing in the poloidal field coils and the ferromagnetic inserts of ITER), deviations from ideal geometry, toroidal field variations, calibration, noise and integration drift.

The proposed methods are applied to the measurement error of the CER, in particular in its high and low operating ranges, as prescribed by the ITER system design description documents, and during transients, which highlight the large time constant related to the shielding of the vacuum vessel.

The analyses presented in the paper show that the design of the CER diagnostic is capable of achieving the requisite performance as needed for the operation of the ITER machine.

Keywords: Rogowski coil, current sensor, statistical measurement error, ITER CER, ferromagnetic inserts, integration drift, calibration

(Some figures may appear in colour only in the online journal)

1. Introduction

On contemporary fusion research facilities based on magnetic confinement, primary control of the machine is based on measurements of the magnetic field surrounding the core of the device. This approach will also be applied on ITER, the tokamak device currently under construction in Cadarache, France, aimed at demonstrating the viability of commercial energy production.

As part of the suite of magnetics measurements on ITER, a Rogowski coil (also known as Chattock–Rogowski coil) [1–7], the Continuous External Rogowski (CER), is included to determine the current flowing in the plasma core and machine structures. This measurement is of high importance due to the very large electromagnetic energy associated with the current in the plasma core. Specifically, the CER provides a measurment of the total toroidal current $I = I_p + I_{eddy}$, where I_p is the plasma current and I_{eddy} is the current induced in the passive structures threading with the CER itself [8–10]. A number of diagnostic systems contribute to the accurate measurement of the plasma current and the toroidal current in ITER: in-vessel and outer vessel coils, high frequency coils, steady-state sensors, continuous flux loops, the CER and the fiber optic current sensor. In particular, the in-vessel tangential coils set provide the reference estimate of I_p for operation. The key role of the CER is to provide a supplementary measure of the toroidal current in quiescent (flat-top) situations, with a single sensor in an uncomplicated, stable, radiation-tolerant and relatively direct fashion, so that it is suitable for ensuring the integrity of the measurement of I_p. For this reason it is an important part in the provision of a safety-relevant measurement of I_p, whose range will be prescribed in the ITER operating license [9]. This role will be integrated within the plasma control system of the machine [9, 11].

The paper addresses a thorough performance assessment of Rogowski coils. It develops by taking the CER as main working example, but the discussed techniques are general and relevant to any application involving Rogowski sensors. Modelling and computational activities are described, which allow to quantify the measurement errors, taking detailed account of the environment. The geometrical complexity of the sensor is accurately accounted for and the standard model which provides the classical expression to compute the flux linkage of Rogowski sensors [4] is considered and quantitatively validated. In order to take into account the non-ideality of the winding, a generalised formula, formally analogue to the classical one, is presented (equation (6)). Models to determine the worst case and statistical measurement accuracies are then provided, which consider the following sources of error:

- approximation of the flux linkage with a discrete sum of fluxes linked with circular turns,
- effects of the joints,
- effects of nearby ferromagnetic components (the ferromagnetic inserts of ITER [12]),
- effects of the eddy currents,
- deviations from ideal geometry of the sensor's windings (deformation and misalignment of the turns, and centricity effect),
- disturbances due to external sources of field (the currents flowing in the poloidal field coils),
- effects of the non ideal geometrical configuration of the threading and non-threading current carrying conductors (calibration using poloidal field coils),
- effect of the toroidal field variations,
- nuclear-induced noise, electronic noise, integration drift.

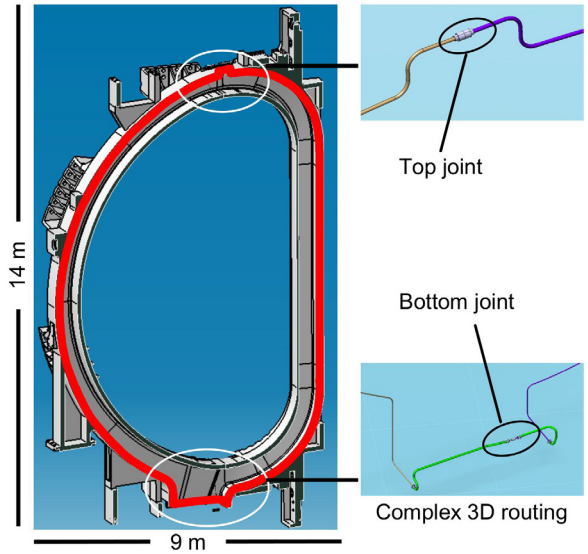

Figure 1. Routing of the CER sensor (bold red line) in a groove cut in the TF coil casing. The insets highlights the complexity of the path. The top joint only has mechanical function, while from the bottom one the two shielded twisted pairs which carry the output signals of the inboard and the outboard part of the sensor emerge.

Within this framework, the measurement error is evaluated, with the aid of a number of suitable operating reference scenario.

The target CER specification define the maximum measurement error in statistical terms as twice the standard deviation σ, in two different operating ranges [10]:

$$2\sigma_{max} = \begin{cases} 1\%, & \text{if } 1\text{ MA} \leqslant I \leqslant 20\text{ MA} \quad \text{high range,} \\ 10\text{ kA}, & \text{if } I \leqslant 1\text{ MA} \quad \text{low range.} \end{cases} \tag{1}$$

The analyses that follow show that such specifications can be met.

2. The CER sensor

A CER sensor is constituted of two halves, the inboard and the outboard parts, each of which consists of two concentric helical windings and is assembled in the form of a cable. The two cables are positioned in a groove cut in the casing of a toroidal field (TF) coil on its outer perimeter, along a complex path (figure 1) designed as a sequence of straight segments and circular arcs [13]. The ends of the two cables are joined together by means of a top and a bottom mechanical joint. The ITER machine will be equipped with three CER sensors,

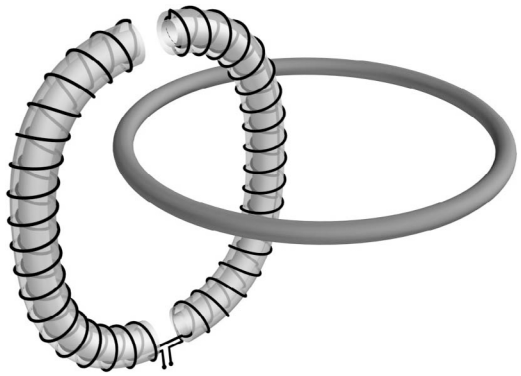

Figure 2. A typical Rogowski coil made of two halves. For convenience of illustration, the windings are represented with a large pitch, and the two mechanical joints which fix the two parts together are not shown. The darker ring represents a conductor carrying the electric current that the sensor is measuring. The inner windings of the inboard and outboard parts are connected in the bottom joint, and the ends of the outer windings constitute the terminals of the sensor. In the case of the CER however, for calibration purposes and for possible use of one half in case of failure of the other half, the two parts are considered as individual sensors. That is to say, instead of realising the electrical connection in the bottom joint, the two halves are put in series by switches in the data acquisition cards.

mounted at different octants, 120 degrees apart toroidally [8]. Figure 2 shows a typical Rogowski coil of the same type of the CER, namely made of two parts and with a double-layer winding. In particular, the electrical connection between the inboard and the outboard windings is accomplished in the bottom joint, while the top joint has mechanical function only. The two half coils are put in series, with the proper polarity. In the case of the CER however, the inner windings of the inboard and outboard parts are not electrically connected in the bottom joint. In fact, for calibration purposes (section 13) and for possible use of one half in case of failure of the other half, the two parts are considered as individual sensors. That is to say, instead of realising the electrical connection in the joint, the two halves are put in series by switches in the data acquisition card, when the diagnostic is operating in measure mode (rather than calibration or other service modes).

The main design specifications and derived parameters of the CER, which were considered for the studies reported in this article, are detailed in table 1. In the final design the routing has been slightly modified in the lower region (the feedout region), including the location of the bottom joint. Such changes do not have any significance with respect to the results we report, as it will be clear from the analyses conducted in the paper.

3. Rogowski model in ideal geometry

For a general Rogowski coil, the flux linkage φ can be calculated in a simple way [4] by making the following two assumptions: (i) the helical nature of the windings is not taken into account, that is the helices are approximated with sequences of independent turns lying in planes perpendicular to the path of the coil; (ii) the magnetic flux density $\boldsymbol{B}$ is considered spatially homogeneous over each cross-section. Hypothesis (ii) is obviously satisfied since the coil's cross-section is small compared to field variations. By comparison with an integral code, we shall see now that (i) is also verified.

If s is the arclength along the coil's path, N the total number of turns in each of the two windings, L the total length, $\lambda = L/N$ the pitch length and $n = 1/\lambda$ the turns density, so that the elemental number of turns is $\mathrm{d}N = n\mathrm{d}s$, the flux is

$$\begin{aligned}\varphi &\cong \int_\gamma n\mathrm{d}s \int_S \boldsymbol{B}\cdot\hat{\boldsymbol{t}}\,\mathrm{d}S \cong nS\int_\gamma \boldsymbol{B}\cdot\hat{\boldsymbol{t}}\,\mathrm{d}s \\ &= \mu_0 Sn\Big(\oint_{\gamma^\circ}\boldsymbol{H}\cdot\hat{\boldsymbol{t}}\,\mathrm{d}s - \int_{\gamma_j}\boldsymbol{H}\cdot\hat{\boldsymbol{t}}\,\mathrm{d}s\Big) \\ &= M_0 I - M_0\lambda(H_{tl}N_l + H_{tu}N_u)\end{aligned} \tag{2}$$

where

$$M_0 = \mu_0 Sn \tag{3}$$

is the nominal mutual inductance, $\gamma = \gamma_i \cup \gamma_o$ the path along the inboard and outboard CER cables, $\gamma_j = \gamma_u \cup \gamma_l$ the two segments corresponding to the upper and lower joints, $\gamma^\circ = \gamma \cup \gamma_j$ the full closed path, $\boldsymbol{H}$ the magnetic field, $\hat{\boldsymbol{t}}$ the unit vector tangent to the path, I the threading current to be measured, N_u and N_l the 'missing' number of turns due to the presence of the joints, H_{tu} and H_{tl} the field tangent to the path at the joints. In short, the model in ideal geometry provides, for a threading current I, the mutual inductance as

$$M = \frac{\varphi}{I} = \mu_0 Sn + \text{joints effect correction} \tag{4}$$

where, as reported in table 1, S is the area corresponding to each single turn (including inner and outer winding turns).

Notice that the values H_{tl} and H_{tu} are due to all the field sources, including the threading current I itself. This is especially relevant in industrial applications, where Rogowski coils with circular shape are quite common, in both variants with single and double layer winding. For them, which typically have only one joint, it is

$$n = \frac{N}{2\pi r - \Delta L} = \frac{N}{(2\pi - \Delta\theta)r}$$

where r is the major radius of the Rogowski and ΔL and $\Delta\theta$ are, respectively, the arc length and angle corresponding to the gap due to the 'missing' turns in the joint region. When a circular Rogowski measures a straight current perpendicular to it and located at its centre, the flux is the same for all turns, hence the flux is N times the flux on each turn, and (2) reads as

$$\varphi \cong NS\frac{\mu_0 I}{2\pi r} - M_0 H^e_{tj}\lambda N_j$$

where N_{tj} and and H^e_{tj} are the missing number of turns and the field tangent to the path due to *external* sources in the joint region. By external we mean all the field sources excluding the current I which is directly threading the coil. Notice again that the conductor which carries the current I has a return path which is external to the coil, and which gives a contribution to H^e_{tj}. This fact is for instance relevant for the calibration of the coil. When the threading current is not in the centre of the circular Rogowski, if the gap due to the joint is not small or

Table 1. Main design parameters of the CER sensor. For illustrative purposes, certain numerical values are artificially shown with a larger number of digits with respect to consistency to the required tolerance.

		Inner winding	Outer winding	Both windings
Winding diameters	(mm)	$2a = 5.5$	$2b = 8.3$	
Pitch length on axis	(mm)	$\lambda = 1$		
Wire diameter	(mm)	0.55		
Path (axis[a]) length	(m)	$L_0 = 38.6344$[a]		
Ideal[a] # of turns		$N_0 = \frac{L_0}{\lambda} = 38\,634.4$[a]		
Missing turns at joints		$N_l, N_u \leqslant 10$		
Total joints length	(mm)	$\Delta L \leqslant 20$		
Length	(m)	$L = L_0 - \Delta L \geqslant 38.6144$		
# of turns		$N = \frac{L}{\lambda} = N_0 - N_l - N_u \geqslant 38\,614.4$		$2N \geqslant 77\,228.8$
Turn density	(m^{-1})	$n = \frac{N_0}{L_0} = \frac{N}{L} = \frac{1}{\lambda} = 1000$		$2n = 2000$
Ideal[a] equivalent area	(m^2)	$N_0 S_a = 0.918$[a]	$N_0 S_b = 2.090$[a]	$N_0 S = 3.008$[a]
Equivalent area	(m^2)	$NS_a = 0.917$	$NS_b = 2.089$	$NS \geqslant 3.007$
Wire lengths	(m)	$L_{wa} \cong 668$	$L_{wb} \cong 1008$	$L_w \cong 1676$
Nominal sensitivity	($\mu H = \frac{Vs}{MA}$)	$M_{0a} = \mu_0 S_a n$	$M_{0b} = \mu_0 S_b n$	$M_0 = \mu_0 S n = 0.097\,847\,258$
Nominal gain factor	($\frac{1}{\mu H} = \frac{MA}{Vs}$)			$\frac{1}{M_0} = 10.220\,010$

[a] For an ideal continuous coil without joints; $S_a = \pi a^2$, $S_b = \pi b^2$, $S = S_a + S_b$.

compensated (see below), the correction term in (2) can be significant, specifically when the threading current is close to the joint.

When there are not threading currents, in (2) it is $I = 0$, and φ is due to the joints effects correction only.

The CER diagnostic consists of the Rogowski loop, the transmission line and the data acquisition card. Since the latter has high input impedance, the acquired voltage signal v is proportional to the rate of change of the flux linkage with the windings, $v = \frac{d\varphi}{dt}$. Time integration and appropriate scaling of v provides the output signal $\mathcal{I}$ of the diagnostic which, in the present case of ideal geometry, has then the very simple expression

$$\begin{aligned}\mathcal{I} &= \frac{\varphi}{M_0} = \int_\gamma \boldsymbol{H}\cdot\hat{\boldsymbol{t}}\,ds = \oint_{\gamma^\circ} \boldsymbol{H}\cdot\hat{\boldsymbol{t}}\,ds - \int_{\gamma_j} \boldsymbol{H}\cdot\hat{\boldsymbol{t}}\,ds \\ &= I - \lambda(N_l H_{tl} + N_u H_{tu}).\end{aligned} \tag{5}$$

We shall see that, in the case of the CER sensor and in ideal geometry, the last equation can be stated as $\mathcal{I} \cong I$ with excellent approximation. However, for general Rogowski coils, the contribution due to the presence of the joints can be significant. Whenever needed, it is possible to compensate their effect by winding a number of additional turns in the proximity of the gaps (e.g. inside the connectors) which substract local fluxes corresponding to the areas SN_l and SN_u.

In order to take into account the unavoidable perturbations from ideal geometry of the windings, we will generalize equation (5). We will then refer to (5) as the *standard or canonical* Rogowski model.

4. Validation of the model in ideal geometry

The model of the CER we will be using for all the analyses performs, in ideal geometry, the (discretised) line integral (5) of the magnetic field $\boldsymbol{H}$ along the CER path, excluding the joints. This is an approximation, since the CER in reality is a double helix rather than a set of circular turns. In order to estimate the accuracy of this simplified model, we used a general integral

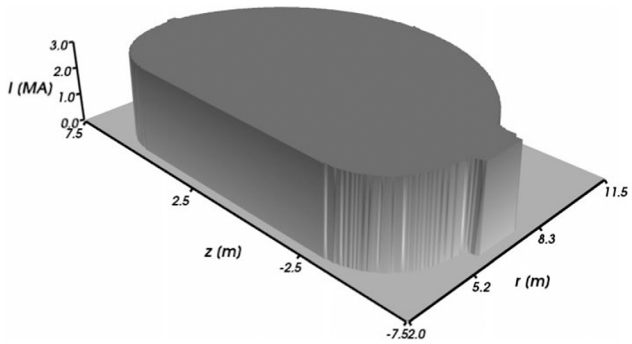

Figure 3. Functional testing of the integral code: calculated CER output due to a $I = 3$ MA threading/non-threading current located at r & z variable over a 60 000 points grid. The effect of the joints is not considered.

code [7], which was configured with the double winding helix defining the CER. The integral code is less versatile and computationally more expensive than the canonical model (5), and it is used only in this section to validate the latter. That is to say, with the aid of the integral code we are able to show that formula (5) calculates the flux linkage with very high accuracy.

Figure 3 visualizes the result of a basic functionality test of the integral code, showing the calculated output of the diagnostic φ/M_0, due to a $I = 3$ MA threading/non-threading current located at r & z variable over a 60 000 points grid, in the case of absence of joints. As numerical examples, we report in table 2 the flux linkage of the CER for a filamentary current $I = 15$ MA located in the centre (the average of the points of the target separatrix, see figure 4) and for various combination of joints. The outputs calculated with both the integral code and with (5) are shown. The agreement between the models is better than 0.2 ppm (about 7 digits agreement) in all the considered cases. The CER sensitivity (mutual inductance) is also shown.

Besides the data reported in table 2, extensive comparison tests were performed to assess the canonical model versus the integral code. In all cases the agreement between the two

Table 2. Flux for $I = 15$ MA calculated with equation (5) and with a general integral code. A substantial 7 digits agreement appears. The presence of the joints affects the 5th digit.

N_u	N_l	N 1 winding	$N\pi(a^2+b^2)$ (m^2)	φ (Wb) Equation (5)	φ_i (Wb) Integral code	$\frac{\varphi-\varphi_i}{\varphi_i}$ Relative difference	$M_i = \frac{\varphi_i}{I}$ $\left(\frac{\mathrm{H}}{10^6} = \frac{\mathrm{Vs}}{\mathrm{MA}}\right)$
0	0	38 634.4	3.0082	1.467 708 870	1.467 709 127	$-0.1751 \cdot 10^{-6}$	0.097 847 27
0	20	38 614.4	3.0067	1.467 423 075	1.467 423 332	$-0.1750 \cdot 10^{-6}$	0.097 828 22
20	0	38 614.4	3.0067	1.467 327 546	1.467 327 803	$-0.1753 \cdot 10^{-6}$	0.097 821 85
10	**10**	38 614.4	3.0067	1.467 375 310	1.467 375 567	$-0.1749 \cdot 10^{-6}$	0.097 825 04
20	20	38 594.4	3.0051	1.467 041 750	1.467 042 007	$-0.1752 \cdot 10^{-6}$	0.097 802 80

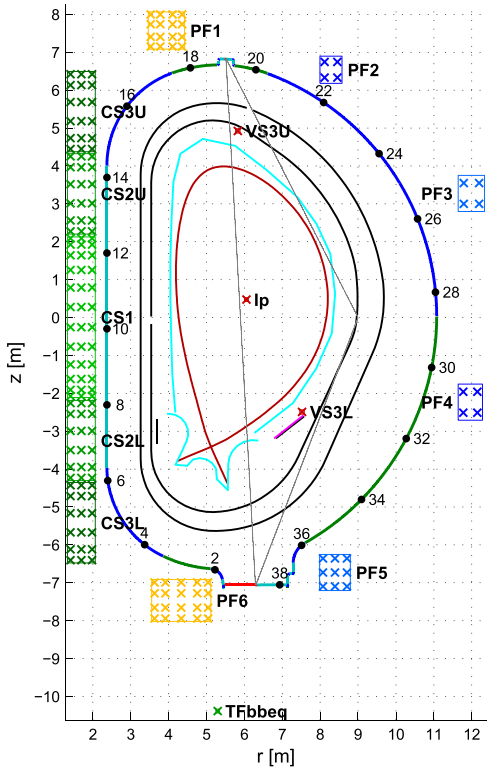

Figure 4. ITER poloidal section, showing the non-threading sources (the CS and PF coils and the equivalent axisymmetric model of the TF busbars), the CER (quoted with the arc length starting at the lower joint), the vessel, the internal VS3 coils, the first wall and the target separatrix. The crosses denote the gauss integration points [14, p 85] used to calculate the field due to the each source. Their configuration is optimal, that is an increase of their number would not increase accuracy. The piecewise straight gray lines ending at the joints are an example of equivalent integration path (see section 13). TFbbeq stands for the TF busbars, implemented as their equivalent axisymmetric model [13, 16]. Adapted with permission from [13].

models is better than 1 ppm. Thus we conclude that the error due to the approximation of the flux linkage with a discrete sum of fluxes linked with circular turns is negligible. The simplified model is then used for all the analyses.

5. Effect of the joints in ideal geometry

The most relevant joints combinations are the following:

- no joints (ideal continuous Rogowski coil)
- $10 + 10$ mm joints (worst case as from CER specifications)
- $5 + 5$ mm joints (about best achievable with reference joints connector design [13, 15]).

5.1. Threading coils

In the worst case specification of $10 + 10$ mm joints, the joints/CER length ratio is $L_j/L \sim 0.5 \cdot 10^{-3}$. Hence we expect a joint effect of such order of magnitude for threading currents. However, a role is also played by the fact that the CER has an elongated shape (figure 4), so that different current configurations imply different effects. Table 3 considers a filamentary current located at three different threading locations, namely the centre (the average of the points of the target separatrix) and the positions occupied by the VS3 coils [13, 16]. The CER output is now expressed in terms of measured current (equation (5)) rather than as flux linkage. We see that indeed the effect of the joints depends on the relative location of the current versus the joints. It is in particular stronger in the case of VS3U, which is comparatively closer to the (upper) joint. The lower part of the table expresses that, in the worst spec case ($10 + 10$ mm joints) the source to source sensitivity differences are about: 550 ppm for I_p versus I_{VS3U}, 100 ppm for I_p versus I_{VS3L}, 450 ppm for I_{VS3U} versus I_{VS3L}. The effect is halved in the case of $5 + 5$ mm joints. The fact that the difference is smaller in the case I_p versus VS3L is somewhat witnessed in figure 5 too, which represents, as functions of the poloidal location, the elemental contributions to the CER signal in ideal geometry due to all the sources shown in figure 4, at their maximum admissible current values [13, 16]. Figure 5 also shows the sum of the contribution of all the external sources. The gray plots give the magnitude of the local magnetic field, whereas the black ones are the aliquot which contribute to the CER signal.

As remarked in section 3, it would be possible to compensate the joints effect. For the CER this is not needed for the following reasons (see also section 5.2 below):

a. the impact on the threading currents is less than an order of magnitude below measurement tolerance specification;
b. the actual joints lengths and their effect can be characterized and compensated (see section 10);
c. unavoidable deviation from the ideal geometry of the CER have a larger impact on the threading currents, as we shall see.

Table 3. Output of the ideal CER, in terms of measured current, due to a filament located in the centre and at the VS3 coils. The sensitivity and the coil to coil sensitivity differences are also shown, as well as the effect of the joints in absolute and relative terms.

Coil	Current I	Joints lengths L_j (mm)	Calculated output $\mathcal{I}_{L_j}$ (MA)	$M_{L_j} = \frac{\varphi}{I} = \frac{M_0 \mathcal{I}_{L_j}}{I}$ (μH $= \frac{\text{Vs}}{\text{MA}}$)	$\mathcal{I}_{L_j} - \mathcal{I}_0$ Joints effect	$M_{L_j}/M_0 - 1$
Plasma[a]	15 MA	0	15.000 000	0.0978 473	—	—
		5 + 5	14.998 295	0.0978 361	−1.70 kA	$-0.114 \cdot 10^{-3}$
		10 + 10	14.996 591	0.0978 250	−3.41 kA	$-0.227 \cdot 10^{-3}$
VS3U[b]	+0.24 MAt	0	+0.240 000	0.0978 473	—	—
		5 + 5	+0.239 908	0.0978 097	−92 A	$-0.383 \cdot 10^{-3}$
		10 + 10	+0.239 816	0.0977 722	−184 A	$-0.767 \cdot 10^{-3}$
VS3L[b]	−0.24 MAt	0	−0.240 000	0.097 8473	—	—
		5 + 5	−0.239 961	0.097 8315	+39 A	$-0.161 \cdot 10^{-3}$
		10 + 10	−0.239 922	0.097 8157	+77 A	$-0.323 \cdot 10^{-3}$
		L_j (mm)	$M_{L_j}^{\text{plasma}}/M_{L_j}^{\text{VS3U}} - 1$	$M_{L_j}^{\text{plasma}}/M_{L_j}^{\text{VS3L}} - 1$	$M_{L_j}^{\text{VS3U}}/M_{L_j}^{\text{VS3L}} - 1$	
Source versus source sensitivity difference		0	0	0	0	
		5 + 5	$+0.270 \cdot 10^{-3}$	$+0.048 \cdot 10^{-3}$	$-0.222 \cdot 10^{-3}$	
		10 + 10	$+0.540 \cdot 10^{-3}$	$+0.096 \cdot 10^{-3}$	$-0.444 \cdot 10^{-3}$	

[a] Implemented as a single filament located at $r = 6.054$ m, $z = 0.474$ m (average of target separatrix points).
[b] Implemented as a single filament; total maximum current in a pulse (4 turns), with pulse duration less than about 0.3 s [13, 16].

5.2. Cross-talk of the non-threading coils

Table 4 reports the cross talk of the non-threading coils with the ideal CER, in terms of measured current and sensitivity, in the worst case condition for the joints (10 + 10 mm). The details of the coils are described in [13, 16]. CS1U and CS1L are considered separately in table 4 for illustrative purpose but, everywhere else in the paper, they are treated as a single source, for they are actually connected in series (figures 4 and 5 also consider a single CS1 coil). As seen in section 3, the output due to non-threading currents in ideal geometry only depends upon the field at the joints locations and on the joints characteristics themselves. Hence the cross talk is due to the presence of the joints (in ideal geometry), and the values shown in table 4 get halved in the case of 5 + 5 mm joints. We see that the TF busbars, implemented as their equivalent axisymmetric model [13, 16], have a tiny effect (15 A), whereas the coils giving the largest contribute (∼3 kA) are PF1 and PF6, which are the closest to the upper and lower joint, respectively. The exact location of the lower joint was not precisely specified at the time the analyses have been performed. We placed it in the centre of the corresponding straight path. For this reason, the calculated outputs corresponding to PF5 & PF6 can be less precise due to possible (minor) differences with respect to the location here considered. This is however not really important. In fact, to the points a,b,c stated in section 5.1 above, we can add the following:

d. the cross talk of the non-threading coils in ideal geometry can be compensated;
e. the deviation from the ideal geometry of the CER have a larger impact on the non-threading currents cross-talk as well (this effect can also be compensated, see section 10).

Then, the cross-talk in ideal geometry reported in table 4, have to be considered mainly as reference information, and not as measurement errors.

6. Measurement error: analysis of the deviation from ideal geometry of Rogowski windings

The manufactured sensor will not be geometrically ideal. In particular, the need of having sufficiently uniformly wound coils was accounted for since the days of the early experimentalists. Citing Chattock (1887) [1]: *'The use of the lathe is the more desirable, as measurements of potential by the helix depend very much for their accuracy upon the uniformity with which it is wound; this being especially the case if its position in the field does not happen to coincide with the direction of the lines of force.'* Analogue statements are found in the current literature [5]. The issue is intuitively clear by imagining e.g. extreme cases of winding non–uniformity. Up to our knowledge, quantitative methods are not available. To formulate the problem, we model the deviations from ideal geometry by considering the following effects:

(i) the variability of the pitch length λ, or equivalently of the turns density $n = 1/\lambda$;
(ii) the variability of the area of the local turns, $S = \pi(a^2 + b^2)$ (including both inner and outer winding turns);
(iii) the turns tilting, described by the colatitude θ and the azimuth ϕ;
(iv) the (non-)centricity effect, due to the fact that the axes of the inner and outer windings will not be exactly coincident; relevant parameters are the local distance between the axes δ and the normal direction to the elemental area

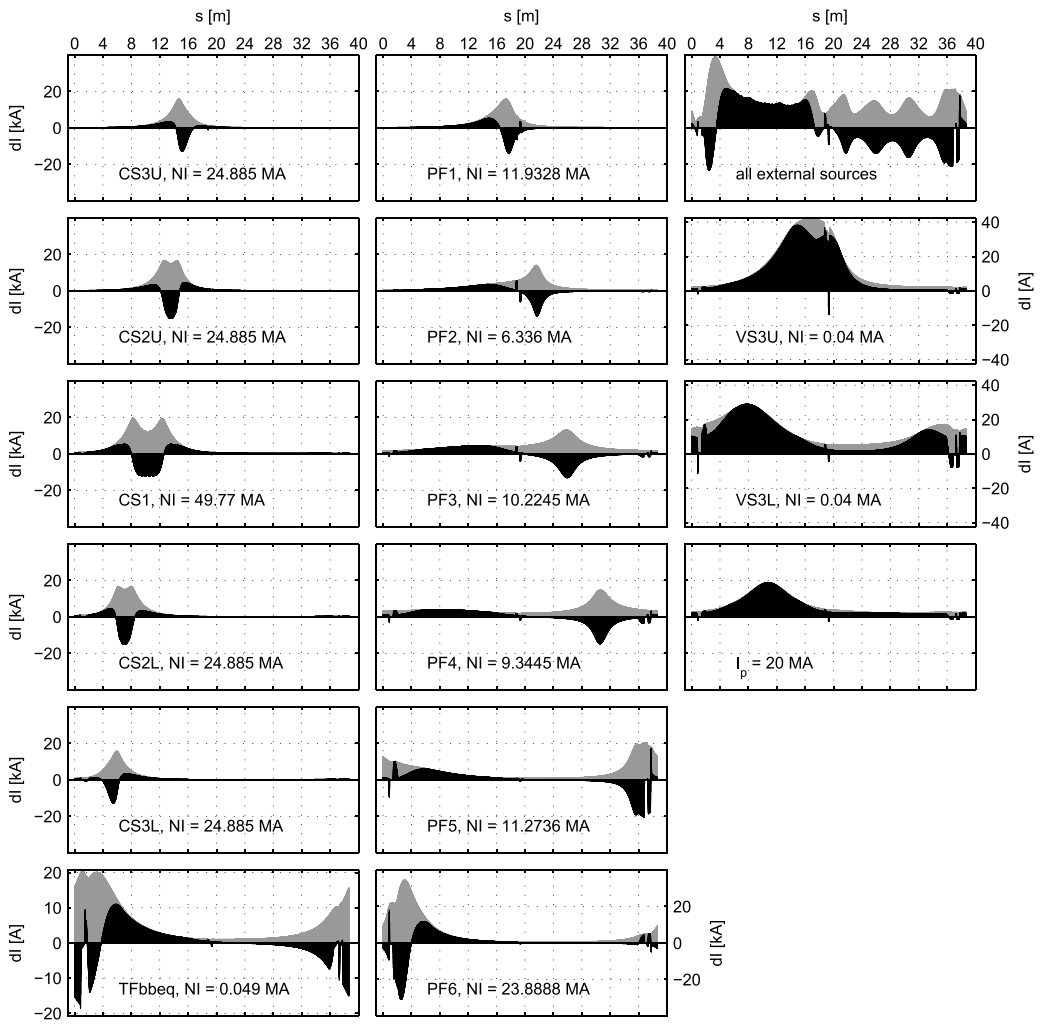

Figure 5. Patterns representing, as functions of the poloidal location, the elemental contributions to the CER signal in ideal geometry due to all the sources shown in figure 4, at their maximum nominal current values [13, 16]. The top-right one refer to the sum of the contribution of all the external sources. The bar graphs in gray and black color represent the magnitude of the local field $|\boldsymbol{H}|\Delta s$ and the aliquot which contribute to the CER signal in ideal geometry $\Delta I = \boldsymbol{H} \cdot \hat{\boldsymbol{t}}\,\Delta s$, respectively. TFbbeq stands for the TF busbars, implemented as their equivalent axisymmetric model [13, 16]. Adapted with permission from [13].

locally defined by the two axes, expressed as another independent azimuth ψ.

All the parameters are functions of the arc length s along the Rogowski path. Then, hereafter, we denote with a ring accent their values corresponding to ideal geometry, e.g. $\mathring{n} = 1/\mathring{\lambda}$ and $\mathring{M}_0 = \mu_0 \mathring{S} \mathring{n}$ are the unperturbed turns density and the ideal sensitivity.

In order to analyze the tilting and the centricity effects, it is needed to define a continuously varying reference frame along the Rogowski path, the trihedral $\{\hat{\boldsymbol{t}}(s), \hat{\boldsymbol{n}}(s), \hat{\boldsymbol{b}}(s)\}$ [17], with respect to which the angle parameters $\theta(s), \phi(s), \psi(s)$ are specified.

The path of the CER is defined as a 3-D sequence of straight and circular segments, which we divided into two main sets, corresponding to the inboard and outboard CER cables, plus two more small segments, representing the joints. Specifically (see also figure 6):

- segments 1–18: inboard CER;
- segment 19: upper joint, with a nominal 10 mm length (worst case);

Table 4. CER output in ideal geometry due to the external axisymmetric coils at their maximum nominal currents [13, 16], in the worst case condition for the joints (10 + 10 mm). The shown values get halved in the case of 5 + 5 mm joints. TFbbeq stands for the TF busbars, implemented as their equivalent axisymmetric model [13, 16]. Adapted with permission from [13].

Coil	N (Turns)	$I_{\max}$ (kA)	$NI_{\max}$ (MAt)	$\mathcal{I}$ (kA)	$M = \frac{\varphi}{NI_{\max}}$ (pH)
CS3U	553	45	24.885	−0.87	−3.42
CS2U	553	45	24.885	−1.03	−4.06
CS1U	553	45	24.885	−0.76	−2.99
CS1L	553	45	24.885	−0.68	−2.67
CS2L	553	45	24.885	−0.75	−2.95
CS3L	553	45	24.885	−0.58	−2.28
PF1	248.6	48	11.933	+3.19	+26.2
PF2	115.2	55	6.336	−0.30	−4.65
PF3	185.9	55	10.225	−1.45	−13.9
PF4	169.9	55	9.345	−1.71	−17.9
PF5	216.8	52	11.274	−1.66	−14.4
PF6	459.4	52	23.889	+2.71	+11.1
TFbbeq	1	49	0.049	+0.015	+29.2

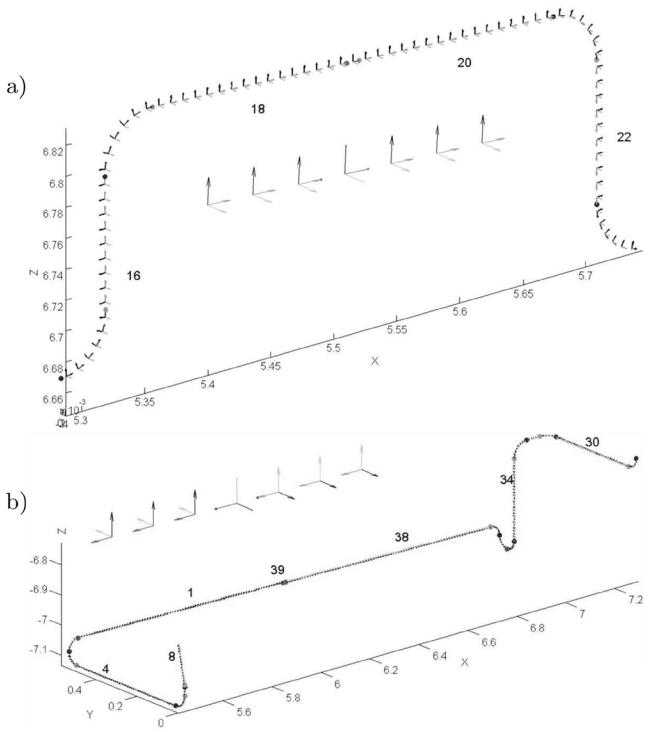

Figure 6. Reference frames defined at the integration points in the upper (*a*) and lower (*b*) joint regions (not to scale, see figures 1 and 4). The numeric labels indicate a selection of the 39 segments with which the various parts of the CER path (inboard/outboard CER and joints) are defined. The magnified insets show the frames across the joints.

- segments 20–38: outboard CER;
- segment 39: lower joint, with a nominal 10 mm length (worst case).

The clearer separation between the inboard and outboard parts of the device allows to consider the two halves as independent sensors, which can be useful in particular for the calibration (section 13) or in case of failure of one half.

The discretized reference we implemented considers 3863 integration points, so that the average step in terms of arc length is $\langle \Delta s \rangle = 1$ cm, with a minimum $\Delta s_{\min} = 7.9$ mm on segment 7. Figure 6 shows the corresponding sequences of trihedrals in the upper and lower joint regions, where the routing is more complex. The unit vectors $\hat{\boldsymbol{t}}, \hat{\boldsymbol{n}}$ are respectively tangent and normal to the path, while the binormal $\hat{\boldsymbol{b}}$ is given by $\hat{\boldsymbol{b}} = \hat{\boldsymbol{t}} \times \hat{\boldsymbol{n}}$. Specifically, on the larger arc segments of the path, we define $\hat{\boldsymbol{n}}$ as having the same direction of $-\frac{\mathrm{d}\hat{\boldsymbol{t}}}{\mathrm{d}s}$ (the opposite of the curvature vector), so that it lies in the poloidal plane and it is outward directed. On the straight segments and on certain arcs in the feedout region, we instead define $\hat{\boldsymbol{n}}$ so that the trihedral is a continuous function of s. This continuity property is preserved along the whole inboard and outboard CER paths and while crossing the upper joint as well (figure 6(*a*)), but not across the lower joint (figure 6(*b*)). The latter is mentioned only for completeness and to state that it does not have any implication. Notice that, since the path is defined as a 3-D sequence of segments, the trihedral could not be analytically determined as the Frenet frame [17], as it would be discontinuous at the knots of the CER path and undefined on the straight segments.

Effects (i) and (ii) act in the same way, thus we define a local gain parameter

$$\kappa = \frac{Sn}{\mathring{S}\mathring{n}}.$$

The turns tilting is analysed with the aid of the unit vectors

$$\hat{\boldsymbol{\tau}} = \cos\theta\,\hat{\boldsymbol{t}} + \sin\theta\,\hat{\boldsymbol{\rho}}, \qquad \hat{\boldsymbol{\rho}} = \cos\phi\,\hat{\boldsymbol{n}} + \sin\phi\,\hat{\boldsymbol{b}},$$

$\hat{\boldsymbol{\tau}}$ being a perturbed version of $\hat{\boldsymbol{t}}$, normal to the turns of the winding. The centricity effect is then formalised by means of a centricity factor ε and a unit vector $\hat{\boldsymbol{\varrho}}$ (normal to the elemental area spanned by the displacement δ between the geometrical axes of the two windings) defined as

$$\varepsilon = \frac{\delta}{\mathring{n}\mathring{S}}, \quad \hat{\boldsymbol{\varrho}} = \cos\psi\,\hat{\boldsymbol{n}} + \sin\psi\,\hat{\boldsymbol{b}}.$$

Given a specific geometric pattern defined by the five quantities $\kappa, \theta, \phi, \delta, \psi$, which are functions of s, the CER output is then expressed as follows

$$\mathcal{I} = \frac{\varphi}{\mathring{M}_0} = \frac{\int_\gamma nS\boldsymbol{B}\cdot\hat{\boldsymbol{\tau}}\,\mathrm{d}s + \int_\gamma \delta\boldsymbol{B}\cdot\hat{\boldsymbol{\varrho}}\,\mathrm{d}s}{\mathring{n}\mathring{S}\mu_0} = \int_\gamma \boldsymbol{H}\cdot\boldsymbol{T}\,\mathrm{d}s \qquad (6)$$

where

$$\boldsymbol{T}(s) = \boldsymbol{T}(\kappa,\theta,\phi,\delta,\psi) = \kappa\hat{\boldsymbol{\tau}}(\theta,\phi) + \varepsilon(\delta)\hat{\boldsymbol{\varrho}}(\psi). \qquad (7)$$

Equation (6) generalises the classical expression (5) and allows to compute the effects due to the nonideal geometry of the winding.

The turns tilting and centricity effects are somewhat similar, since they both cause pickup of perpendicular flux. In the case of the CER, the values of the involved parameters (see next section) imply that the error due to the centricity effect always is a small fraction of the tilting one (section 9).

7. Measurement error: statistical model

The measurement error is evaluated in statistical fashion in terms of twice its standard deviation [10, 13]. The error will then be denoted as 2σ. To determine it, we consider:

- N_{cp} total control points along the routing: 4 of them are fixed (the initial and final ends of the two half CER cables), while the remaining ones are randomly located, with uniform distribution, along the inboard and outboard CER paths ($N_{\mathrm{cp}}/2 - 2$ for each half CER);
- f_s = spatial frequency of the geometric deviations $= 1/\langle \Delta s \rangle = 1/$(average spacing among control points);
- all the geometric deviation parameters are randomly generated at each control point, and then interpolated at each integration point (a C^1 interpolation scheme is applied in order to avoid overshoots).

We take the local gain parameter, κ, as normally distributed with mean 1 and a standard deviation, σ_κ, to be specified. The turns tilting colatitude, θ, and the centricity displacement,

δ, are also given normal distributions, but with mean 0, and certain standard deviations, σ_θ and σ_δ. The azimuth tilting and centricity parameters, ϕ and ψ, need instead to be uniformly distributed in the interval $[-90, 90]$ deg. That spans the 4 quadrants, since θ and δ take positive and negative values. To determine σ_κ, σ_θ and σ_δ, we consider that, for a normal random variable with standard deviation σ, the interval $[-3\sigma, +3\sigma]$ corresponds to 0.9973 probability, essentially 100% of the whole distribution. For the local gain, measurements were made on prototypes [18], which suggest to take 2% as maximum deviation. From the CER cable specifications, we then take 0.5 mm as maximum centricity displacement. And, since there are not information about realistic maximum deviation of the tilting colatitude angle, we need to leave it as a parameter. The maximum geometric deviations are also used to calculate the theoretical worst case errors. In summary, the quantities of the statistical model which we consider known are (wc stands for worst case):

$$
\begin{aligned}
|\pm \Delta\kappa_{\rm wc}| &= \Delta\kappa_{\rm max} = 3\sigma_\kappa = 0.02\\
|\pm \delta_{\rm wc}| \quad &= \delta_{\rm max} \quad = 3\sigma_\delta = 0.5 \text{ mm}\\
|\pm \phi_{\rm max}| &= |\pm \psi_{\rm max}| = 90 \text{ deg}
\end{aligned}
$$

whereas the quantities that we leave as parameters are f_s and σ_θ. Specifically, the statistical error is mainly calculated on the following grid of values:

$$
\begin{aligned}
&f_s = \tfrac{1}{\langle \Delta s\rangle} = \{0.2, 2, 5, 20\} \text{ m}^{-1} \text{ (control points per meter)},\\
&|\pm \theta_{\rm wc}| = \theta_{\rm max} = 3\sigma_\theta = \{1, 2, 4, 8\} \text{ deg}.
\end{aligned}
$$

We speculate that $\theta_{\rm max} = 8$ deg is an extreme and unrealistic condition, and consider $f_s = 0.2$ control points per meter as the limiting and unlikely condition for the spatial frequency parameter, since it implies local systematic geometric deviations.

8. Measurement error: worst case analysis

Besides the statistical error, it is interesting to evaluate the worst case theoretical error(s). Their determination is performed by considering a *minimization geometrical pattern* and a *maximization geometrical pattern*, for which the CER output is respectively minimized and maximized. The analysis is specific for each of the three effects considered.

The minimum output $\mathcal{I}_{\rm min}$ due to non-ideal local gain is obtained by applying a 2% reduction to all the elemental contributions (single turn fluxes) which are positive, and a 2% increase where they are negative. Vice versa for the maximum output $\mathcal{I}_{\rm max}$. It turns out that the error (the difference between the min/max output and the output in ideal geometry $\mathring{\mathcal{I}}$) is the same in absolute value for the min and max cases.

For the tilting effect, the maximum (minimum) output is obtained when the normal to each turn is rotated as much as possible towards (away from) the direction of the local magnetic field. In this case the error is not the same in absolute value for the min and max cases.

The centricity effect, like the tilting, imply a pickup of the flux perpendicular to the path of the CER. The maximizing procedure consists of evaluating, at each integration point, the elemental flux through the area $\lambda\delta_{\rm max}$ due to the projection of the field in the plane determined by the normal and binormal directions. Unlike the tilting, and like the local gain, the centricity error is the same in absolute value for the min and max cases.

Table 5. Calculated measurement error 2σ in the case of flat-top plasma configuration and in presence of the ferromagnetic inserts, parametrised versus the spatial frequency of the geometrical deviations f_s and the maximum tilting angle θ_{max}. The values in italic font correspond to the limiting region of the parameters that we consider unrealistic. Just for completeness, we report that the calculation were performed with the worst case joint configuration ($10 + 10$ mm).

Flat-top, $I_{\rm p} = 15$ MA Contributions: plasma+CS+PF+FI (TF substracted due to integration)				
Total statistical error (5000 runs) due to all geometric deviations ($\Delta\kappa_{\rm max} = 0.02$, $\delta_{\rm max} = 0.5$ mm, $\theta_{\rm max}$ parameter)				
$\theta_{\rm max} = 3\sigma_\theta$		$\frac{100\cdot 2\sigma(\mathcal{I}_{\rm p}+\mathcal{I}_{\rm coils}+\mathcal{I}_{\rm FI})}{I_{\rm p}}$ (%)		
1°	*0.94*	0.45	0.29	0.15
2°	*1.09*	0.55	0.36	0.19
4°	*1.54*	0.83	0.57	0.29
8°	*2.68*	*1.51*	*1.04*	*0.54*
$\approx f_s = \frac{1}{\langle \Delta s\rangle}$ (m^{-1})	*0.2*	2	5	20
$N_{\rm cp}$	*10*	76	190	760

9. Computation of the measurement error: effect of the ferromagnetic inserts

In the present and in subsequent sections we apply the proposed methods to compute numerically the measurement errors. We do that for the CER sensor with the aid of a number of suitable operating reference scenario. These constitute a very small subset of case, which obviously are not intended to be representative as a catalogue of the most important reference scenarios of the ITER machine, and which are are fully sufficient to evaluate the performances of the CER diagnostic. This will be clear from the outcome of all the analyses we will perform. We anticipate the main reasons, which are the following. Firstly, recall that (see section 1) the ITER design description documents [9, 10] specify that the CER is not intended to be used during transients. Its function is to measure $I_{\rm p}$ in steady-state condition. This is due to the shielding of the vacuum vessel (VV). We will assess the measurement error in two different flat-top configurations and will se that the measurement error is the same. This result is due to a more general property. In fact, it is a known experimental evidence that Rogowski loops are quite effective current sensors, meaning that they provide a reliable and accurate measure of the total current threading the loop itself and are essentially insensitive to the current density distribution and to its time variation properties (for variations within the sensor's bandwidth, which is clearly the case, due

Table 6. Detail of the calculated measurement error for the flat-top plasma configuration, and for the specific case where the maximum tilting angle is $\theta_{max} = 2$ deg, parametrised versus the spatial frequency of the geometrical deviations f_s. Reading code: italic font correspond to the limit region of the f_s parameter that we consider unrealistic; in bold are negligible errors due to the FI; boxed values represent errors that can significantly be reduced by means of poloidal field compensation (section 10).

					Statistical analysis (5000 runs)											
					$f_s \approx \frac{1}{4.8\ \mathrm{m}} \approx 0.2\ \mathrm{m}^{-1}$ $N_{cp} = 10$				$f_s \approx \frac{1}{50\ \mathrm{cm}} = 2\ \mathrm{m}^{-1}$ $N_{cp} = 76$				$f_s \approx \frac{1}{5\ \mathrm{cm}} = 20\ \mathrm{m}^{-1}$ $N_{cp} = 760$			
Contribution (@ flat top) of	Kind of geometric deviation	Worst case $\Delta\mathcal{I}_{min}$ (kA)	Worst case $\Delta\mathcal{I}_{max}$ (kA)	Worst case $\frac{100\Delta\mathcal{I}}{I_p}$ (%)	$\Delta\mathcal{I}_{min}$ (kA)	$\Delta\mathcal{I}_{max}$ (kA)	2σ (kA)	$\frac{100\cdot 2\sigma}{\mathcal{I}_p}$ (%)	$\Delta\mathcal{I}_{min}$ (kA)	$\Delta\mathcal{I}_{max}$ (kA)	2σ (kA)	$\frac{100\cdot 2\sigma}{\mathcal{I}_p}$ (%)	$\Delta\mathcal{I}_{min}$ (kA)	$\Delta\mathcal{I}_{max}$ (kA)	2σ (kA)	$\frac{100\cdot 2\sigma}{\mathcal{I}_p}$ (%)
Plasma 15 MA	*nS*	±564		3.8	−288	+286	131	*0.87*	−123	+125	62	0.41	−47	+39	20	0.13
+CS+PF	tilting	−654	+637	4.3	−197	+198	94	*0.63*	−101	+125	54	0.36	−41	+31	19	0.13
(TF substracted	centricity	±119		0.79	−38	+41	18	*0.12*	−21	+21	10	0.07	−6	+8	4	0.02
Due to integration)	all				−302	+295	163	*1.09*	−163	+152	83	0.55	−59	+45	28	0.19
	nS	±1.2		0.008	−0.70	+0.66	0.37	*0.002*	−0.29	+0.27	0.14	0.001	−0.09	+0.07	0.04	0.0003
FI @ $I_p = 15$ MA	tilting	−1.9	+1.9	0.013	−0.70	+0.72	0.37	*0.002*	−0.36	+0.40	0.18	0.001	−0.11	+0.11	0.06	0.0004
(∼scale with I_p)	centricity	±0.353		0.0023	−0.17	+0.16	0.07	*0.0004*	−0.14	+0.14	0.03	0.0002	−0.03	+0.01	0.01	0.0001
	all				−0.93	+1.02	0.53	*0.003*	−0.49	+0.45	0.23	**0.002**	−0.15	+0.12	0.07	**0.0005**

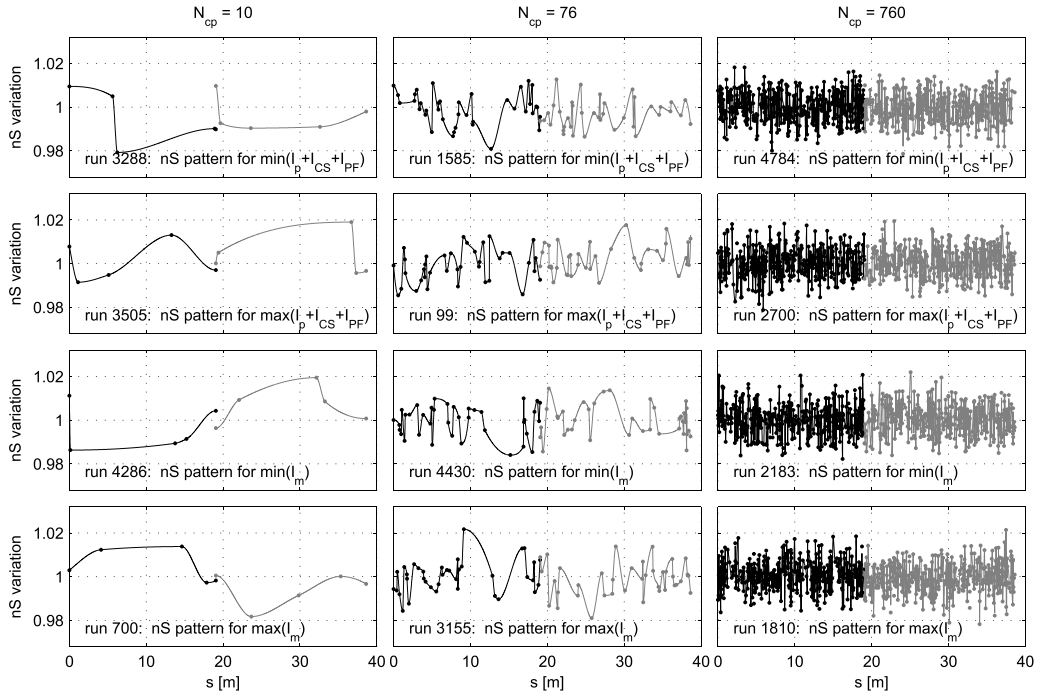

Figure 7. Patterns corresponding to the minimum and maximum measurement error on the output of the CER signal in a statistical set consisting of 5000 runs, in the case of flat-top plasma configuration with presence of the ferromagnetic inserts. The local gain *nS* is randomly varying, while the other parameters are set to the values they have in ideal geometry. The plots in the first and second rows refer to the contribution of the source plasma+CS+PF, whereas the third and fourth rows consider the FI contribution. For the first, second and third column it is respectively $f_s \approx 0.2,\ 2,\ 20$ control points per meter.

to the large time constant of the VV shielding (figure 9)). Our methods consent to confirm this evidence in quantitative terms and provide a precise and complete performance assessment. In particular we will show that the computed measurement error is essentially the same in all considered cases and does not change for different plasma and eddy current configurations (see e.g. figure 14).

In this section we evaluate the measurement errors in ideal and non-ideal geometric configuration of the CER, for a flat-top configuration with plasma current $I_\mathrm{p} = 15$ MA. The input data, represented by the total field $\boldsymbol{H}(\boldsymbol{r})$, were obtained with a 3-D numerical model [19–21], which implements an iterative procedure based on an integral formulation and includes the ferromagnetic inserts (FI) of ITER [12]. In order to indicate all the considered contributions, the error in non-ideal geometry will be denoted as $2\sigma(\mathcal{I}_\mathrm{p} + \mathcal{I}_\mathrm{coils} + \mathcal{I}_\mathrm{FI})$, and in similar way in subsequent sections.

9.1. Ideal CER geometry

In the ideal case of unperturbed geometry of the CER windings, in the output signal there will be a contribution of the FI due to the presence of the joints. The CER is an inductive sensor whose output voltage v is the time derivative of the flux linkage. The measured current is obtained by scaling and time-integrating the voltage v. Since the toroidal field current has the same value before and during pulses, and the integrator is reset at the beginning of the pulse, the actual measured output is given by

$$\Delta\mathcal{I} = \mathcal{I}_1 - \mathcal{I}_0 = \frac{\varphi_1 - \varphi_0}{\mathring{M}_0} = \frac{1}{\mathring{M}_0}\int_{t_0}^{t_1} v(t)\mathrm{d}t,$$

where $\mathcal{I}_1$ and $\mathcal{I}_0$ are the calculated outputs respectively at flat-top and before the start of the pulse. This is possibly relevant because the FI provide a contribution off pulse as well. We specifically get, in ideal geometry and with $10 + 10$ mm joints: $\mathcal{I}_{m0} = 0.012$ A (pre-pulse contribution to the calculated CER output due to the magnetization); $\mathcal{I}_{m1} = -11.8$ A (contribution to the calculated CER output at flat-top due to the magnetization). Thus the aliquot in the output due to the FI is $\Delta\mathcal{I}_m = \mathcal{I}_{m1} - \mathcal{I}_{m0} = -11.8$ A. For the typical plasma current $I_\mathrm{p} = 15$ A, we get $\Delta\mathcal{I}_m/I_\mathrm{p} = -0.79 \cdot 10^{-6}$. The effect of the ferromagnetic insert in ideal geometry is then less than 1 ppm (halved for $5 + 5$ mm joints), hence it is negligible.

9.2. Perturbed CER geometry

Table 5 shows the total measurement error $2\sigma(\mathcal{I}_\mathrm{p} + \mathcal{I}_\mathrm{coils} + \mathcal{I}_\mathrm{FI})$, calculated with the statistical model described in section 7, and parametrised versus the spatial frequency of the geometrical deviations f_s and the maximum tilting angle θ_max. All the geometric effects are considered and act simultaneously and independently. As expected, the error decreases with f_s. We can see that, apart from the results corresponding to limit/unrealistic values of the parameters (in italic font), the error due to the non-ideal geometry of the CER is below 1%. We will show that this error can significantly be reduced, for the contribution of the CS and PF coils can be compensated.

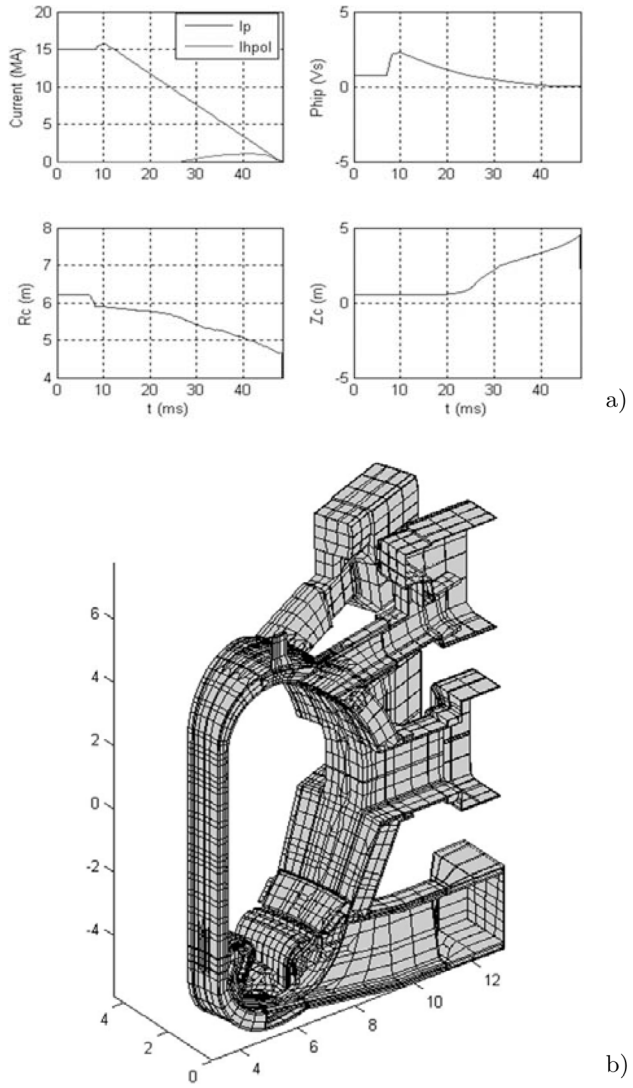

Figure 8. (*a*) The MD UP PFV scenario. I_p and I_{hpol} are the plasma and the poloidal halo currents respectively. The former decreases rapidly from 15 MA to zero. Φ_p is the diamagnetic flux, and R_c, Z_c give the position of the plasma current centroid. (*b*) numerical model.

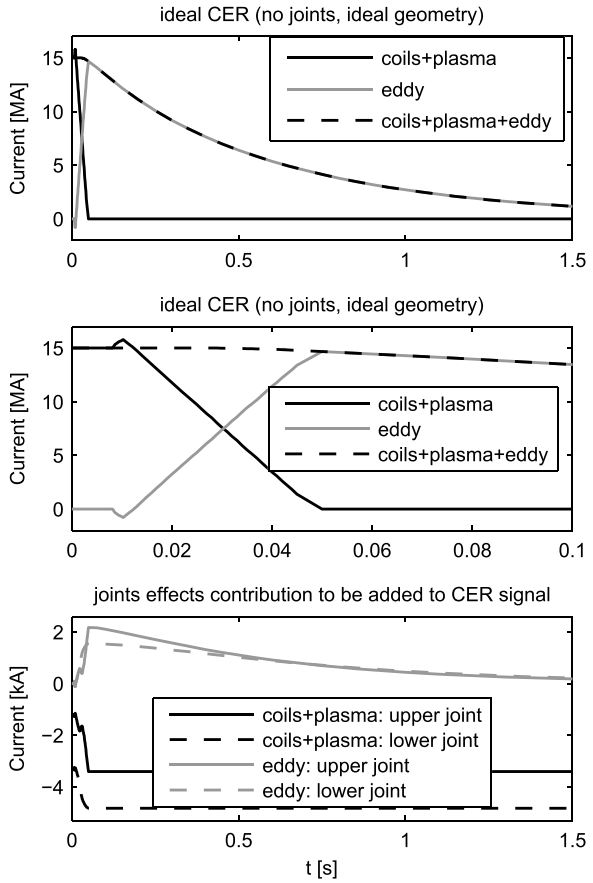

Figure 9. Contributions to the calculated CER output in ideal geometry for the MD UP PFV scenario. The middle plot gives a zoomed view of the top one in the range 0–100 ms. When I_p start decreasing, the eddys start to rise so that their sum, namely the CER output, remains approximately constant during the event. Hence the CER cannot be used as a direct measure of I_p in general conditions. More specifically, from the first plot one can estimate of the VV toroidal time constant as $\tau_{VV} \approx 0.5$ s. Thus, during transient or fast events, the CER become aware of them $\sim$0.5 s after they arise. The CER is not intended to be used during transients. The reference estimate of I_p for operation is provided by the in-vessel tangential coils [9]. Adapted with permission from [13].

Table 6 provides more details in the specific case where the maximum tilting angle is $\theta_{max} = 2$ deg. The worst case and the statistical errors are reported, when each geometric effect acts individually as well. Unlike the global view of table 5, which takes all the sources into account (plasma + CS + PF + FI) at once, here the ferromagnetic inserts are separately analyzed, leading to the conclusion that their effect to the measurement error is negligible in non-ideal CER geometry too.

Since the FI are saturated by the toroidal field, for them the equivalent linear permeability model in the poloidal direction [22, 23] holds. Thus the FI contribution to the measurement can be evaluated by such model. That implies that the FI contribution approximately scales with I_p. Hence, the error due to the FI is negligible in the case of pulses with lower plasma current as well.

Table 6 also let us appreciate that the error due to the centricity effect is small (even smaller after CS&PF compensation, see next section). Indeed, as anticipated in section 6, the values of the involved parameters imply that the centricity error is a fraction of the error due to turns tilting. Specifically, it is about 1/6 of the error due to a maximum tilting $\theta_{max} = 3\sigma_\theta = 2$ deg. This is a general result, not limited to the case considered in the present section.

It is interesting to visualize the patterns corresponding to the minimum and maximum measurement error on the output of the CER signal in the considered statistical set, consisting of 5000 runs. In the example shown in figure 7 the local gain nS is randomly varying, while the other parameters are set to the values they have in ideal geometry. The first and second parts of each plot, respectively drawn in black and gray color, correspond to the inboard and outboard CER cables. The dots represent the N_{cp} control points. The plots in the first and second rows refer to the contribution of the source plasma + CS + PF, whereas the third and fourth rows consider the FI contribution. For the first, second and third column it is respectively $N_{cp} = 10, 76, 760$, namely $f_s \approx 0.2, 2, 20$ control points per meter.

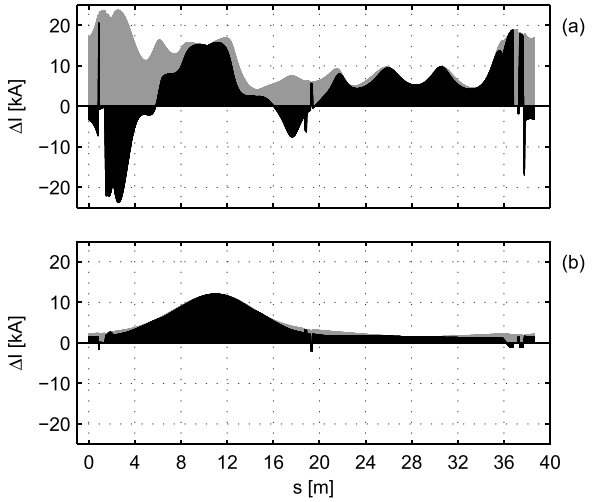

Figure 10. Elemental contributions to the CER signal in ideal geometry, as functions of the poloidal location, in the MD UP PFV scenario. The configuration considered is the one at the instant $t = 50$ ms, where the eddy currents provide the maximum effect, $\mathcal{I} = \mathcal{I}_{\rm eddy} = 14.7$ MA, and it is $\mathcal{I}_{\rm p} = 0$. In (a) the contributions of both the eddy currents and the poloidal field coils are considered, while in (b) the eddies act alone. The bar graphs in gray and black color represent the magnitude of the local field $|\boldsymbol{H}|\Delta s$ and the aliquot which contribute to the CER signal in ideal geometry $\Delta I = \boldsymbol{H}\cdot\hat{\boldsymbol{t}}\,\Delta s$, respectively.

Table 7. Calculated measurement error $2\sigma(\cdot)$ for the MD UP PFV scenario, parametrised versus the spatial frequency of the geometrical deviations and the maximum tilting angle, before and after CS/PF compensation. The values in italic font correspond to the limit region of the parameters that we consider unrealistic, while the values in bold are a sensible upper bound estimate of the error due to the CER geometric imperfections. For completeness we report that the calculation were performed with the worst case joint configuration (10 + 10 mm).

	MD UP PFV					
	Flat top			Max eddy		
Configuration	$t = 0$ s $I_{\rm p} = 15$ MA $I_{\rm eddy} = 0$			$t = 0.05$ s $I_{\rm p} \approx 0$ $I_{\rm eddy} = 14.7$ MA		
Total statistical error (5000 runs) due to all geometric deviations ($\Delta\kappa_{\max} = 0.02$, $\delta_{\max} = 0.5$ mm, $\theta_{\max}$ parameter)						
Before CS & PF compensation	$\frac{100\cdot 2\sigma(\mathcal{I}_{\rm p}+\mathcal{I}_{\rm coils})}{\mathcal{I}_{\rm p}+\mathcal{I}_{\rm coils}}$ (%)			$\frac{100\cdot 2\sigma(\mathcal{I}_{\rm eddy}+\mathcal{I}_{\rm coils})}{\mathcal{I}_{\rm eddy}+\mathcal{I}_{\rm coils}}$ (%)		
2°	*1.23*	0.64	0.21	*1.25*	0.65	0.22
4°	*1.85*	1.00	0.34	*1.89*	1.02	0.35
8°	*3.51*	*1.83*	*0.63*	*3.39*	*1.87*	*0.64*
After CS & PF compensation	$\frac{100\cdot 2\sigma(\mathcal{I}_{\rm p})}{\mathcal{I}_{\rm p}}$ (%)			$\frac{100\cdot 2\sigma(\mathcal{I}_{\rm eddy})}{\mathcal{I}_{\rm eddy}}$ (%)		
2°	*0.74*	0.29	0.09	*0.74*	0.29	0.09
4°	*0.79*	**0.33**	0.11	*0.79*	**0.33**	0.10
8°	*0.96*	*0.48*	*0.15*	*0.95*	*0.47*	*0.15*
$\theta_{\max} = 3\sigma_\theta$	0.2	2	20	0.2	2	20
$\approx f_s = \frac{1}{\langle\Delta s\rangle}$ (m^{-1})						

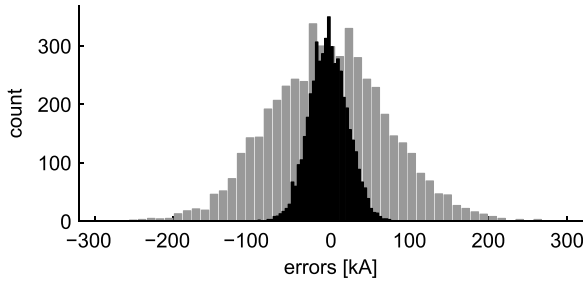

Figure 11. Error distributions of the MD UP PFV configuration at $t = 50$ ms considered in table 7, for $f_s = 2$ m^{-1} and $\theta_{\max} = 3\sigma_\theta = 4$ deg. The histogram in gray colour correspond to the errors obtained by considering the combined effects of the eddy currents and the CS&PF coils; the one in black colour takes into account the eddies only, hence it refers to the actual error after CS&PF compensation.

10. Computation of the measurement error during transients, poloidal field compensation and statistical error distribution

In this section we estimate the effect of the eddy currents on the measurement error. The performed computations show that, as anticipated in section 9 and as expected from a well engineered Rogowski coil, the CER performances do not depend on the characteristics of the threaded current distribution (see also the results reported in section 11). We then analyze how the measurement error improves significantly by compensating the contribution due to the poloidal field coils. The use of the first instants of the simulation allows to get such result for the flat top configuration as well. This result is also reflected into corresponding changes of the statistical error distribution.

The input data $\boldsymbol{H}(\boldsymbol{r}, t)$ we consider correspond to the scenario MD UP PFV (Major Disruption Up, Poloidal Field Variation), and were obtained with a 3-D numerical model [19–21]. We chose this configuration because it is an important one, as it implies a very short (<50 ms) current quench [11], and because it consents to show in a clear way the shielding properties of the VV. Figure 8(a)) depicts the time-evolution of the main quantities (plasma and halo currents, diamagnetic flux, position of the plasma current centroid). The numerical model (figure 8(b)), which is made of 8519 elements and has 9848 discrete degrees of freedom, includes: vessel inner and outer shell; copper cladding; ribs; upper, equatorial, lower port extension; rail; cassettes; inner vertical targets; outer vertical targets; dome. The first two plots in figure 9 show the contribution of the relevant sources to the calculated CER output in ideal geometry, and a zoom in the range 0–100 ms. The eddy currents give the max contribution at $t = 50$ ms. From $t = 50$ ms onwards it is $I_{\rm p} = 0$. Notice that, when $I_{\rm p}$ start decreasing, the eddys start to rise so that their sum, namely the CER output, remains approximately constant during the event. Hence the CER cannot be used as a direct measure of $I_{\rm p}$ in general conditions. More specifically, from the first plot in figure 9, one can estimate the toroidal time constant of the vacuum vessel (VV) as $\tau_{\rm VV} \approx 0.5$ s. Thus, during transient or fast events, the CER become aware of them about 0.5 s after they arise. As stated in the introduction, the CER is not intended to be used

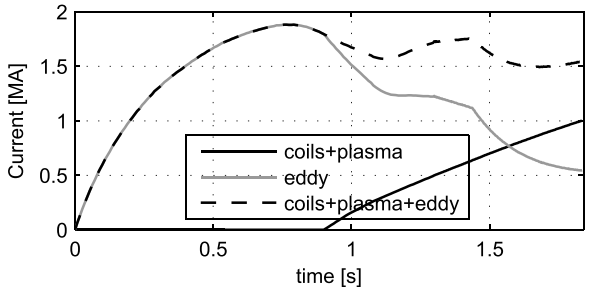

Figure 12. Time evolution of the plasma current, the eddy current and their sum, in the considered breakdown & ramp-up scenario, calculated as line integral of the corresponding magnetic field along the CER path in ideal geometry and without joints. The field used to calculate the plasma current includes the contribution due to the currents flowing in the CS/PF coils which, however, have no effect, for those coils are external to the CER path. The VS3 coils give no contribution as well (exactly only in ideal geometry and without joints), since they are connected in anti-series.

during transients for measuring I_p. The reference estimate of I_p for operation is provided by the in-vessel tangential coils [9]. In the last plot of figure 9 the calculated effect of the joints is shown: the eddys goes to zero asymptotically, whereas the presence of the joints themselves imply that the contribution due to the CS and PF coils, which are essentially constant throughout the scenario, remain present in the output.

Figure 10 represents the contributions to the CER signal as functions of the poloidal location. The gray plots show the magnitude of the local magnetic field, whereas the black ones are the aliquot which contribute to the CER signal in the case of ideal geometry. The configuration considered is the one at $t = 50$ ms, where the eddy currents provide the the maximum effect, $\mathcal{I} \cong \mathcal{I}_{eddy} = 14.7$ MA, and it is $\mathcal{I}_p = 0$.

In the case of the flat top configuration ($t = 0$), for which $\mathcal{I} \cong \mathcal{I}_p = 15$ MA, the patterns (not shown) are nearly identical to the one shown in figure 10. In both cases the measured quantity (the total toroidal current) is about the same. In general, however, patterns are different (figure 14).

Figure 10(a) includes the cross talk of the CS and PF coils, whereas in figure 10(b) only the contribution of the eddy currents is considered. The latter is then relevant when considering the output signal of the CER, after applying a compensation technique. In fact, the ideal CS/PF cross talk and the additional CS/PF cross talk due to CER imperfections can be compensated (see [23] and references therein). Since the measurement error of the CS/PF current is small (the corresponding 2σ is estimated to be 0.2%), the CS/PF compensation works effectively (0.2% of the cross talk is negligible). Table 7 reports the total measurement error 2σ, parametrised versus the spatial frequency of the geometrical deviations and the maximum tilting angle, in two panels labeled before and after CS&PF compensation. All the geometric effects are considered and act simultaneously and independently. The compensation of the poloidal field currents greatly reduce the measurement error due to the geometric non-idealities of the device, which is thus below 1% even for the limit/unrealistic values of the parameters. The error for realistic values of the CER geometric imperfection parameters should be less than 0.33%. This value might still be conservative, however there

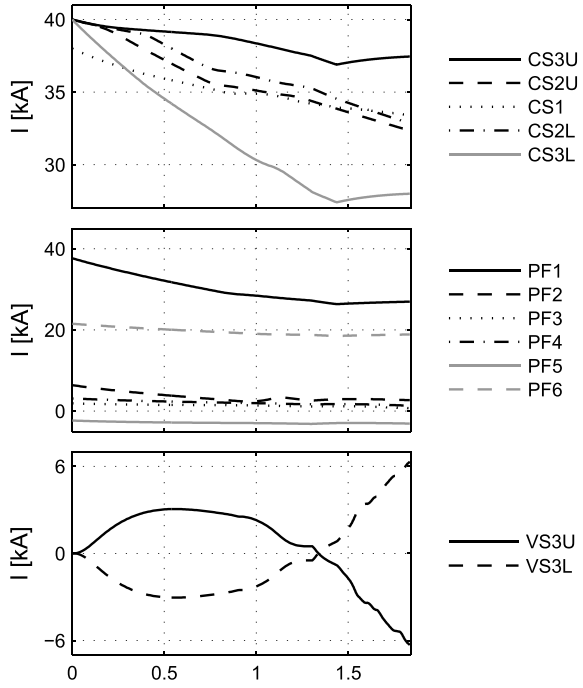

Figure 13. Currents in the poloidal field coils for the considered breakdown & ramp-up scenario.

are no absolute certainties on that, as it will depend on the final properties of the as-installed CER cables.

Notice that the calculated errors before compensation at $t = 0$ are not the same as for the flat-top configuration we analysed in the previous section (table 5). This is because the poloidal field currents are different.

Figure 11 shows the error distributions of the flat top configuration considered in table 7 for $f_s = 2$ m^{-1} and $\theta_{max} = 3\sigma_\theta = 4$ deg. The gray and black histograms correspond to the errors before and after CS&PF compensation, respectively.

The results of the present section remain valid for the more general MD UP scenario, where a toroidal field variation is present as well, because these effects are less important.

11. Computation of the measurement error at low range

We assess now the measurement accuracy at low current values, in particular in the low operating range, defined by the condition that the total toroidal current and the maximum measurement error do not exceed 1 MA and 10 kA, respectively (see (1)).

The CER works in the low measurement range only during breakdown, hence we consider a typical breakdown & ramp-up scenario. As seen in section 9 and 10, the shielding of the VV and the properties of Rogowski sensors, imply that this analysis is fully sufficient to assess the performances at low range. Figure 12 shows the time evolution of the plasma current, the eddy current and their sum, calculated as line integral of the corresponding magnetic field along the CER path in ideal geometry. Relevant instants of interest are (time expressed in seconds, current in MA):

Table 8. Calculated measurement error $2\sigma(\cdot)$ for the considered breakdown & ramp-up scenario, parametrised versus the spatial frequency of the geometrical deviations and the maximum tilting angle, before and after CS/PF/VS3 compensation. The values in italic font correspond to the limit region of the parameters that we consider unrealistic, whereas the values in bold are a sensible upper bound estimate of the error due to the CER geometric imperfections. For completeness we state that the calculation were performed with the worst case joint configuration (10 + 10 mm).

	Breakdown			Ramp-up	
	$t = 0.081$ s	$t = 0.198$ s	$t = 0.765$ s	$t = 1.300$ s	$t = 1.833$ s
Configuration	$I_p = 0$	$I_p = 0$	$I_p = 0$	$I_p = 0.5$ MA	$I_p = 1$ MA
	$I_{eddy} = 0.5$ MA	$I_{eddy} = 1$ MA	$I^{max}_{eddy} = 1.88$ MA	$I_{eddy} = 1.23$ MA	$I_{eddy} = 0.54$ MA
				$I_{tot} = 1.73$ MA	$I_{tot} = 1.54$ MA

Total statistical error (5000 runs) due to all geometric deviations ($\Delta\kappa_{max} = 3\sigma_\kappa = 0.02$, $\delta_{max} = 3\sigma_\delta = 0.5$ mm, $\theta_{max} = 3\sigma_\theta$ parameter)

Before CS & PF & VS3 compensation

	$2\sigma(\mathcal{I}_p + \mathcal{I}_{eddy} + \mathcal{I}_{coils})$ (kA) (low range)							$\frac{100\cdot 2\sigma(\mathcal{I}_p+\mathcal{I}_{eddy}+\mathcal{I}_{coils})}{\mathcal{I}_p+\mathcal{I}_{eddy}+\mathcal{I}_{coils}}$ (%)										
2°	*27*	25	9.5	*25*	25	18	9.3	*1.4*	1.2	0.47	*1.39*	1.34	0.95	0.50	*1.60*	1.47	1.05	0.55
4°	*47*	43	16	*45*	41	30	16	*2.2*	2.1	0.78	*2.30*	2.25	1.61	0.84	*2.67*	2.47	1.77	0.95
8°	*91*	*81*	*30*	*86*	*79*	*57*	*29*	*4.2*	*3.9*	*1.5*	*4.34*	*4.28*	*3.07*	*1.59*	*5.05*	*4.70*	*3.37*	*1.75*

After CS & PF & VS3 compensation

	$2\sigma(\mathcal{I}_{eddy})$ (kA) (low range)							$\frac{100\cdot 2\sigma(\mathcal{I}_p+\mathcal{I}_{eddy})}{\mathcal{I}_p+\mathcal{I}_{eddy}}$ (%)										
2°	*3.7*	1.4	0.43	*7.3*	2.7	1.7	0.84	*0.72*	0.27	0.08	*0.73*	0.27	0.17	0.08	*0.75*	0.29	0.18	0.09
4°	*3.8*	**1.5**	0.48	*7.5*	**2.9**	1.9	0.94	*0.75*	**0.30**	0.10	*0.76*	**0.30**	0.19	0.10	*0.78*	**0.32**	0.21	0.10
8°	*4.3*	*1.9*	*0.64*	*8.5*	*3.8*	*2.5*	*1.3*	*0.86*	*0.40*	*0.13*	*0.87*	*0.41*	*0.26*	*0.13*	*0.91*	*0.44*	*0.28*	*0.14*
$\theta_{max} = 3\sigma_\theta$	0.2	2	20	0.2	2	5	20	0.2	2	20	0.2	2	5	20	0.2	2	5	20
	$\approx f_s = \frac{1}{\langle\Delta s\rangle}$ (m^{-1})																	

- Breakdown ($0 < t < 0.900$):
  - $t = 0.081$: $I_p = 0$, $I_{tot} = I_{eddy} = 0.5$
  - $t = 0.198$: $I_p = 0$, $I_{tot} = I_{eddy} = 1.0$
  - $t = 0.765$: $I_p = 0$, $I_{tot} = I_{eddymax} = 1.88$
- Ramp-up ($0.900 \leqslant t$):
  - $t = 0.900$: $I_p = 0-$, $I_{tot} = I_{eddy} = 1.79$
  - $t = 1.300$: $I_p = 0.5$, $I_{tot} = 1.73$
  - $t = 1.833$: $I_p = 1.0$, $I_{tot} = 1.54$

Figure 13 reports the poloidal field coil currents throughout the scenario. We notice that, during breakdown and ramp-up, while the total toroidal current is small, most of the CS&PF currents are large (only PF2–PF5 are not that large). Hence, before poloidal field coils compensation, the statistical error is expected to be relatively high. That is indeed the case, as quantitatively shown in table 8, which reports the total measurement error $2\sigma(\cdot)$, parametrised versus the spatial frequency of the geometrical deviations and the maximum tilting angle, in two panels labeled *before* and *after* CS&PF&VS3 compensation. All the geometric effects are considered and act simultaneously and independently. The after compensation error values are calculated by considering only the magnetic field due to the plasma and the eddy currents. Therefore, since in this scenario the VS3 currents are also activated, to be rigorous we mention that the compensation procedure targets the VS3 coils too. In fact, although the VS3U and VS3L coils are connected in anti-series, the non-ideality of the CER implies that the error before compensation depends upon I_{VS3} as well. This effect amount to a fraction of a kA at the maximum I_{VS3} in pulsed condition, which, compared to the error due to the PF&CS coils, is very small. I_{VS3} is quite small at $t = 0.081$ s, hence the error due to possibly uncompensated VS3 would be negligible, as follows for comparison with the after compensation error at the beginning of the breakdown (table 8).

During the low measurement range of the breakdown phase, the plasma current is zero and thus the CER output is only due to the eddy currents. The corresponding measurement error for realistic values of the CER geometric imperfection parameters is, according to table 8, expected to be less than 40 kA. This value might still be conservative, however there are no certainties on that, as it will depend on the final properties of the as-installed CER cables. The same result, $2\sigma < 40$ kA, holds for the remaining part of the breakdown and during ramp-up as well.

The measurement error can however dramatically be reduced. As already noticed, in fact, the ideal CS/PF/VS3 cross talk and the additional CS/PF/VS3 cross talk due to CER imperfections can be compensated. The effects of the CS/PF/VS3 currents on the FI gets compensated too, because, as explained in section 9.2, for the FI the equivalent linear poloidal permeability model holds. As seen in the previous section, since the 2σ parameter of the CS/PF/VS3 current measurement is small, the compensation works effectively.

The other effects due to CER non-idealities and to the FI, are roughly proportional to the plasma current and to the toroidal vessel current (hence they decrease when the total toroidal current gets smaller). Then, after performing the poloidal field coils compensation, even when considering the unrealistic cases (8 deg of maximum tilt and/or $f_s = 0.2$), the statistical error is within specification (table 8).

Figure 14 represents the contributions to the CER signal at all the poloidal locations for the time instants corresponding to the breakdown and ramp-up configurations considered in table 8, after CS/PF/VS3 compensation. The gray plots show the magnitude of the local magnetic field, whereas the black ones are the aliquot which contribute to the CER signal in ideal geometry.

We notice that the result 2σ equal or less than about 0.30% shown in table 8 holds for the flat top and max eddy configurations analysed in section 9 and 10 as well. Hence such result is a general property of the CER diagnostic. As anticipated, this is due to the fact that well engineered loop Rogowski sensors provide a reliable measure of the total enclosed current, and the measurement error is approximately uniform regardless of the specific current density distribution. Our analyses confirms such property and consents qualitative and quantitative assessments.

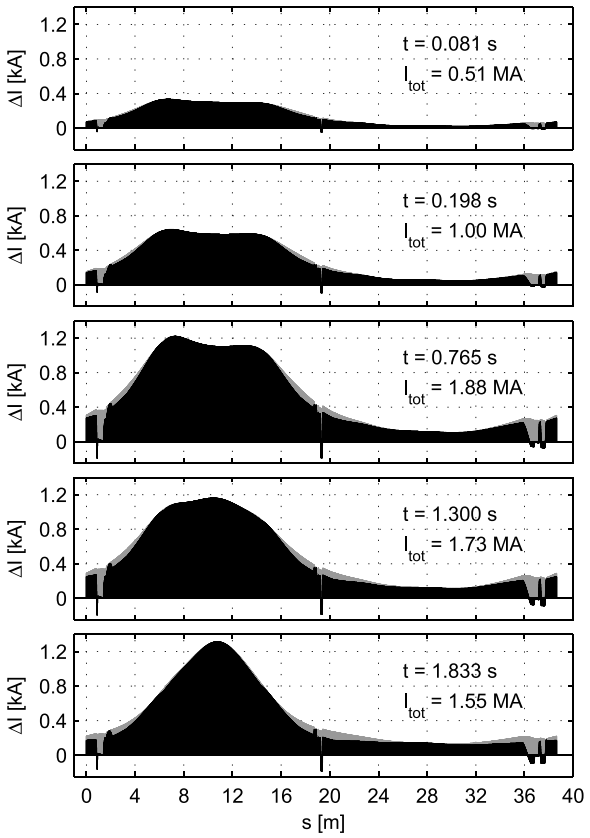

Figure 14. Elemental contributions to the CER signal in ideal geometry, as functions of the poloidal location, in the considered breakdown & ramp-up scenario. The bar graphs in gray and black color represent the magnitude of the local field $|\boldsymbol{H}|\Delta s$ and the aliquot which contribute to the CER signal in ideal geometry $\Delta I = \boldsymbol{H} \cdot \hat{\boldsymbol{t}}\, \Delta s$, respectively. The configuration considered are those for which quantitative results are reported in table 8 (after CS&PF&VS3 compensation panel). The different shapes and magnitudes in the five plots reflect the eddy and plasma current distribution. Despite these differences, the measurement error is always approximately the same.

12. Computation of the measurement error: effect of toroidal field variations

In this section we assess whether the variations of the toroidal field (TF) caused by the plasma paramagnetism (ramp-up at low beta-poloidal) and subsequent diamagnetism (heating to high beta) could affect the CER measurement. In fact it is not a-priori clear if such variations are effectively eliminated by the TF power supply. If not, the possibility for pick-up effects, especially due to the non-ideality of the CER, arises.

The CER lies on the external perimeter of the TF coil, mostly in its poloidal symmetry plane. Since the TF solenoid is not toroidally continuous, the field due to the TF current along the CER path is not negligible.

The solenoid is not very far from being toroidally continuous in the inward region. Thus the field at the CER location in such region is much less than 1 T at $I_{\rm TF} = 68$ kA, which is the TF coil nominal current [13, 16]. The field is instead much stronger (more than 3 T at $I_{\rm TF} = 68$ kA) in the external part of the outward region. These fields estimates have been obtained with both simple filamentary models and accurate 3D calculations, which resulted to be in good agreement with each other.

Only a fraction F of the TF field at the maximum $I_{\rm TF}$ current value has to be considered in order to calculate the CER measurement error due to the possible non-ideal rejection properties of the TF power supply. The following considerations consent to estimate F.

The maximum plasma diamagnetic flux [25] (with poloidal beta $\beta_{\rm pol} = 3$) is $\Phi_p = 3.6$ Vs, whereas the flux linkage with one turn of the TF coil is about 500 Vs at $I_{\rm TF} = 68$ kA. The ratio between this flux and Φ_p is then more than 100, and thus a maximum Φ_p variation will not cause more than a 1% $I_{\rm TF}$ variation. Hence we can take $F = 0.01$ but this is a very conservative assumption.

The field is mostly toroidally directed (this is less true in the lower feedout region only), hence it is perpendicular to the CER path. The pick-up is then essentially due to turns tilting, and not much by the local gain (pitch and cross section) variations. The centricity effect also implies pick-up of perpendicular field, but, as repeatedly remarked, it is less significant than the tilting.

Like in the previous sections, the measurement error is calculated by assuming: the maximum centricity deviation, $\delta_{\rm max} = 3\sigma_\delta = 0.5$ mm; the maximum local gain deviation, $\Delta\kappa_{\rm max} = 3\sigma_\kappa = 2\%$; the maximum tilting angle, $\theta_{\rm max} = 3\sigma_\theta = \{2, 4, 8\}$ deg. 8 deg is considered a limit and unrealistic value. For smaller (or larger, but not too much larger) tilting angles, the error scales linearly with very good approximation.

Many statistical analyses were performed, each of which considers a different value of the spatial frequency of the

Table 9. Inboard, outboard and full CER outputs, due to the external and internal axisymmetric coils, in ideal geometry and at maximum nominal currents. Quantities are calculated with the *simple model*. Specifically, for the inboard and outboard CER, line integral along straight lines connecting the joints are performed (figure 4). For the full CER, the field at the joints only is considered for the external coils, whereas for the threaded sources (VS3U-L & Ip) the field at the joints gives a correction. The values represented with bold font in the central and right panels refer to the sources (PF2–PF5) which provide the largest outputs and sensitivities, and which are not the ones with the largest available $NI_{\max}$ (bold in left panel). The latter provide instead comparatively small outputs (italic font). PF1 and PF6 also provide small outputs, which moreover show appreciable inboard versus outboard differences.

					Ideal CER **& ideal coils geometry**, CER with $10+10$ mm joints						
					Absolute outputs				Gains		
					Inboard	Balanced	Outboard	Full	Inboard	Outboard	Full
	N	$I_{\max}$	$NI_{\max}$	Gauss	$\mathring{\mathcal{I}}_i$	$\frac{\mathring{\mathcal{I}}_i-\mathring{\mathcal{I}}_o}{2}$	$\mathring{\mathcal{I}}_o$	$\mathring{\mathcal{I}}$	$\frac{\mathring{\mathcal{I}}_i}{NI_{\max}}$	$\frac{\mathring{\mathcal{I}}_o}{NI_{\max}}$	$\frac{\mathring{\mathcal{I}}}{NI_{\max}}$
Coil	(Turns)	(kA)	(MAt)	Points	(kA)				(kA MAt^{-1})		
CS3U	553	45	**24.885**	$3\cdot6$	−225.99	*−225.56*	+225.12	−0.87	−9.0814	+9.0465	−0.035
CS2U	553	45	**24.885**	$3\cdot6$	−339.30	*−338.78*	+338.27	−1.03	−13.635	+13.593	−0.041
CS1	1106	45	**49.770**	$3\cdot12$	−669.55	*−668.83*	+668.11	−1.44	−13.453	+13.424	−0.029
CS2L	553	45	**24.885**	$3\cdot6$	−296.37	*−296.00*	+295.62	−0.75	−11.910	+11.879	−0.030
CS3L	553	45	**24.885**	$3\cdot6$	−202.98	*−202.69*	+202.40	−0.58	−8.1566	+8.1333	−0.023
PF1	248.6	48	11.933	$4\cdot4$	*+254.08*	*+252.49*	*−250.89*	+3.19	+21.293	−21.025	+0.268
PF2	115.2	55	6.336	$2\cdot2$	+2 950.0	**+2 950.1**	−2950.3	−0.30	**+465.59**	**−465.64**	−0.047
PF3	185.9	55	10.225	$2\cdot2$	+5 237.7	**+5 238.4**	−5239.1	−1.45	**+512.27**	**−512.41**	−0.142
PF4	169.9	55	9.345	$2\cdot2$	+5 062.8	**+5 063.7**	−5064.5	−1.71	**+541.80**	**−541.98**	−0.183
PF5	216.8	52	11.274	$3\cdot3$	+5 323.2	**+5 324.0**	−5324.9	−1.66	**+472.18**	**−472.33**	−0.147
PF6	459.4	52	**23.889**	$5\cdot4$	*−49.450*	*−50.807*	*+52.163*	+2.71	−2.0700	+2.1836	+0.114
VS3U	4	10[a]	0.040	1	*30.816*		*9.154*	*39.969*	770.39	228.84	999.23
VS3L	4	10[a]	0.040	1	*30.073*		*9.914*	*39.987*	751.82	247.86	999.68
Ip[b]	1		**20**	1	16 730.1		3265.3	19 995.5	836.51	163.27	999.77

[a] VS3 steady state max rms current [13, 16], available for both operation (anti–series connection) and calibration (co–series or parallel).
[b] Modeled with a single filament @ $[r\,z] = [6.054\ \ 0.474]$ m (average of target separatrix points).

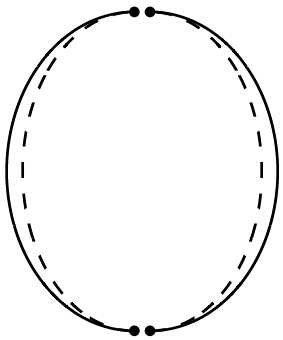

Figure 15. Schematization of the ideal and real path of the CER.

geometric variations, f_s, and the three geometric deviation types, acting both separately and simultaneously. Tilting is indeed predominant. The worst result gives an error $2\sigma = 14$ kA. It corresponds to $f_s = 0.2$ control points per meter (and $\theta_{\max} = 8$ deg), implying a local systematic tilting effect, which is unlikely to happen. A more realistic case is with $f_s = 2$ control points per meter and $\theta_{\max} = 4$ deg, for which the error is $2\sigma = 2.5$ kA. Detailed numerical results are reported in [13].

13. Calibration

A specific scenario and the procedure for the calibration of the CER are in progress to be defined and agreed [10]. In this section we describe the relevant work performed during the design review activities of the diagnostic [24]. Further studies will be carried out in the future.

A natural way to perform the calibration of the diagnostic is to use the VS coils, acting one at a time or in co-series, because they are internal to the whole CER loop (figure 4). However, since the CER is constituted of two parts, T Todd proposed to calibrate the two halves separately, by using the external CS and PF coils. This idea dates back to the original Chattock's proposal [1], later reissued by Rogowski and Steinhaus [2, 3], who meant the sensor as a general open device, and not necessarily a closed loop. We refer to the two calibration types as VS3 calibration and split calibration. The latter conveys the following advatages:

- the signals are much larger than those available when using the VS3 coils (table 9);
- better compliance: simultaneously recording the three analog signals (inboard CER, outboard CER and their sum), or acting on the CER connections is less dangerous or at least much simpler than acting on the VS3 coils configuration (co-series, anti-series);
- suitable combinations of CS/PF currents can provide indications of local CER imperfections after installation;
- the calibration with the VS3 coils connected in series instead of anti-series is feasible anyway.

A deviation from the ideal path would not have any relevant effect. In fact, the ideal and the real CER paths (inboard/

outboard) constitute closed loops which do not link any current (figure 15). Hence the line integral only depends on the initial and final ends of the CER cable, i.e. the locations of the joints, and a survey of the as-installed CER is not needed. The need of knowing the exact location of the joints is relevant only with reference to the very close coils (mainly PF6 and PF1).

The non-ideal geometric configuration of the CS and PF coils may impact the accuracy of the split calibration method. With respect to that, an ad-hoc dry run would allow to calibrate using 11 independent sources (5 CS and 6 PF coils), which would reduce the rms error by a factor of more than three, not to mention that the two halves provide two opposite signals. We shall however see that this is likely not needed, because the non-ideal configuration of certain coils (PF3, PF4 and CS1) has very little impact.

In order to compare the two calibration methods, namely using the CS/PF versus using the VS3 coils, we need to calculate the inboard, outboard and full CER output due to each poloidal field source. That means calculating line integrals along the inboard and outboard CER path. We recall figure 5, which shows the elemental contributions to the CER signal in ideal geometry due to all the sources as functions of the poloidal location along the CER path.

Alternatively to the CER path, equivalent integration paths can be used, the simplest being piecewise straight lines connecting the end of the joints (see figure 4). To perform the analysys, we then use the following *simple model*:

- for non-threading sources (CS and PF coils):
  - $\mathring{\mathcal{I}}_i$ & $\mathring{\mathcal{I}}_o$: ideal inboard & outboard CER outputs, calculated as line integral along straight lines ending at the joints;
  - $\mathring{\mathcal{I}}_i + \mathring{\mathcal{I}}_o + \mathring{\mathcal{I}}_j = 0$ ($\mathring{\mathcal{I}}_j =$ line integral along upper + lower joints);
  - $\mathring{\mathcal{I}}_{\text{split}} = \mathring{\mathcal{I}}_i + \frac{\mathring{\mathcal{I}}_j}{2} = -\mathring{\mathcal{I}}_o - \frac{\mathring{\mathcal{I}}_j}{2} = \frac{\mathring{\mathcal{I}}_i - \mathring{\mathcal{I}}_o}{2} = \frac{\mathring{\mathcal{I}}_i}{|\mathring{\mathcal{I}}_i|}\frac{|\mathring{\mathcal{I}}_i| + |\mathring{\mathcal{I}}_o|}{2}$: balanced quantity, obtained by adding half of the 'missing' fluxes at the joints;
  - $\mathring{\mathcal{I}} = \mathring{\mathcal{I}}_i + \mathring{\mathcal{I}}_o = -\mathring{\mathcal{I}}_j$: full CER output (for which only the field at the joints matters);
- for threading sources:
  - $\mathring{\mathcal{I}} = \mathring{\mathcal{I}}_i + \mathring{\mathcal{I}}_o$: full CER output ($\mathring{\mathcal{I}} = NI - \mathring{\mathcal{I}}_j$ for VS3 coils and $\mathring{\mathcal{I}} = I_p - \mathring{\mathcal{I}}_j$ for plasma; the field at the joints gives a small correction to the threaded current).

We remark that the quantities considered in the simple model are computed with the canonical model (5), namely without considering the CER imperfections. This is adequate because the effect of the CER imperfections on the output signals in calibration and in measure mode are correlated and do not have to be considered twice. This can be explained as follows. The calibrated measure is $Y = \mathcal{I}/k$, where k is the calibration coefficient obtained by performing a specific calibration scenario, e.g. a dry run with known current flowing in the VS3 coils. Both $\mathcal{I}$ and k deviate from their ideal values $\mathring{\mathcal{I}}$ and $\mathring{k} = 1$. Since both deviations have the same physical root (the CER geometric nonidealities), an increase in $\mathcal{I}$ would correspond to an increase in k. The relative deviation on the calibrated output is $\frac{\Delta Y}{\mathring{Y}} = \frac{\Delta \mathcal{I}}{\mathring{\mathcal{I}}} - \frac{\Delta k}{\mathring{k}}$. The statistical error on Y in terms of its standard deviation is then $\sigma_Y = \sqrt{\sigma_{\mathcal{I}}^2 + \sigma_k^2 - 2c\sigma_{\mathcal{I}}\sigma_k}$ where c is the correlation coefficient. The ideal and unrealistic cases of full correlation and incorrelation provide $\sigma_Y = |\sigma_{\mathcal{I}} - \sigma_k|$ and $\sigma_Y = \sqrt{\sigma_{\mathcal{I}}^2 + \sigma_k^2}$, respectively. In the (unreasonable) latter case, $2\sigma_{\mathcal{I}} \approx 2\sigma_k \approx 0.3\%$ (table 8) would give $2\sigma_Y \approx 0.4$, while the former implies quite a small error. Then the estimate of the total measurement error as given in section 15 is correct. As stated, a complete quantitative analysis of this matter will be carried out in the framework of a future study, after the calibration procedure is defined.

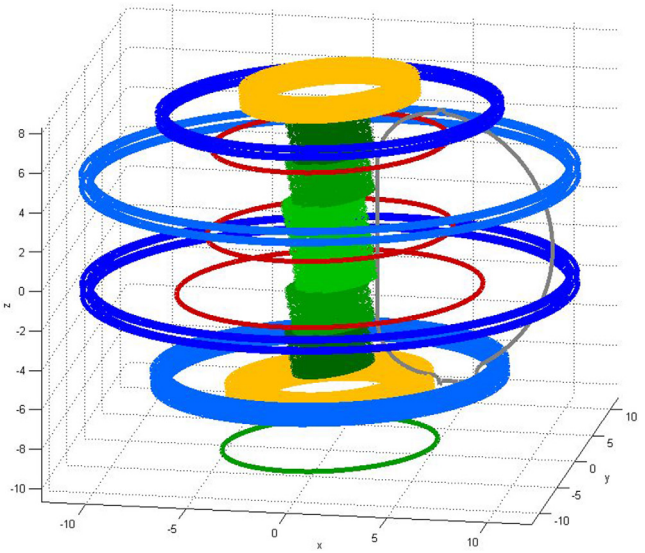

Figure 16. Illustration of the considered poloidal field sources, represented as sets of Gauss filaments (see figure 4), in the nonideal case where each coil is tilted of an amount corresponding to an (exaggerated) $\Delta z_{\max} = -0.3$ m in the azimutal direction $\phi = 180$ deg.

Table 9 reports the quantitative details for the case where the poloidal field coils are in their ideal geometric configuration. The magnetic fields were calculated by considering an optimal number of gauss points, as shown in figure 4. The absolute outputs correspond to the maximum available currents [13, 16]. The lower part of the table mainly accounts for the calibration using the threading VS3 coils, whereas the other results are especially interesting when considering the calibration with the non-threading CS&PF coils. The coils with the largest sensitivities (right part of table 9) are PF2–PF5, which show about 50 times higher values than the other CS/PF coils (despite the larger $NI_{\max}$ available to the latter). In turn, the absolute outputs of the other CS/PF coils are an order of magnitude higher than the VS3 coils. Hence, as expected, comparatively the VS3 coils produce very small absolute outputs. The outputs of the inboard and outboard CER parts are roughly coincident for all the external coils but PF1 and PF6, which are the closest to the joints. It is then advisable to use in general the reported balanced signal, namely the algebraic average of the two outputs which, as seen, is analytically the same of e.g. the sum of the inboard signal plus half of the 'missing' fluxes at the upper and lower joints.

Table 10. Output variations of the ideal CER due to non-ideal geometric configurations of the current sources. Values represented with bold font qualify the coils which are particularly suitable to be used for split calibration. Framed values refer to errors larger than 0.5%.

Ideal CER with 10 + 10 mm joints							
Perturbed geometry of poloidal field sources							
	Vertical Shift Δz (mm)	Horizontal shift Δx (mm)	Horizontal shift Δy (mm)		Tilt $\Delta z_{max} = -5$ mm @ ϕ (deg)		
Coil	±10	±5	+5	−5	0, 180	+90	−90	
	Percent variation on *split* CER calculated outputs, $\Delta\mathring{\mathcal{I}}_i$, $\Delta\mathring{\mathcal{I}}_o$ (%)							
CS3U	∓0.41	±0.18	±0.002		±0.69	∓0.005		
CS2U	∓0.05	±0.15	±0.002		±0.25	∓0.005		
CS1	± 0.02	**±0.11**	± 0.004		± 0.02	∓0.01		
CS2L	±0.08	±0.13	±0.009		∓0.22	∓0.02		
CS3L	±0.32	±0.14	±0.01		∓0.56	∓0.05		Inboard CER
PF1	±1.8	±0.68	∓0.002		∓1.3	±0.002		or
PF2	∓0.19	∓0.01	$\mp 3 \times 10^{-4}$		±0.07	$\pm 1 \times 10^{-4}$		Outboard CER
PF3	**∓0.05**	∓0.02	$\mp 6 \times 10^{-4}$		± 0.01	$\mp 2 \times 10^{-4}$		
PF4	**±0.03**	∓0.02	∓0.001		∓0.009	∓0.001		
PF5	±0.22	∓0.02	∓0.001		∓0.09	∓0.007		
PF6	±19	∓2.8	∓0.26		∓13	∓1.1		Inboard CER
	±18	∓2.6	∓0.24		∓12	∓1.1		Outboard CER
	Percent variation on *full* CER calculated output, $\Delta\mathring{\mathcal{I}}$ (%)							
VS3U[a]	$\mp 4 \times 10^{-4}$	$\pm 5 \times 10^{-5}$	-2×10^{-7}	$+3 \times 10^{-7}$	$\pm 2 \times 10^{-4}$	$+3 \times 10^{-8}$	-8×10^{-8}	
VS3L[a]	$\pm 6 \times 10^{-5}$	$\pm 2 \times 10^{-5}$	$\mp 1 \times 10^{-6}$		$\mp 2 \times 10^{-5}$	$\mp 2 \times 10^{-6}$		

[a] Modeled with a single filament.

The results shown in table 9 also highlight the fact that different sources give output CER signals with very different magnitudes. In particular, the output due to the VS3 coils is in the kA range, to be compared to the MA range which is typical when the CER is in measure mode. This is to be taken into account for the design of the data acquisition cards, in order not to lose numerical accuracy in calibration mode.

Since a huge number of other magnetic diagnostics are available in the ITER machine (in particular internal and external pick-up coils and saddle loops), it is certainly possible to have a good knowledge of the field along a path connecting the initial and final ends of half CER. With reference to that, it is important to characterize the sensitivity of the CER signals with respect to the real location of the sources (the 11 CS and PF coils). A quantitative analysis has thus been performed to determine the variation of the outputs of the two half CER and of the full CER due to the unknown exact geometric configuration of the CS/PF/VS3 coils. In particular the following effects were considered:

i. rigid vertical displacement of each coil of ±10 mm;
ii. rigid horizontal displacement of each coil in the x and y direction of ±5 mm;
iii. tilt of each coil with respect to the z axis of an appropriate angle so that the point of the coil reaching the minimum z position has a $\Delta z = -5$ mm with respect to the centre (the calculation was repeated for the cases of the tilt applied in the azimutal directions $\phi = \{0, 90, 180, 270\}$ deg;
iv. independent shift of the upper/lower joints from their ideal location.

Figure 16 shows the considered sources in a tilted configuration, exaggerated for illustrative purposes. The results of the analysis are reported in table 10. In particular, the central part of the table refer to the split inboard/outboard CER output, for which:

- the sources to which correspond the least variation in the outputs of the two half CERs are PF3 & PF4, with errors in the range 0.02 to 0.05%;
- small variations correspond to CS1 as well, with a maximum deviation of 0.11% corresponding to a Δx shift of ±5 mm;
- split output variations for VS3 coils are not considered, since they will not be normally used for split calibration.

Concerning the full CER output (lower part of the table), we have:

- the non-ideal geometric configuration of the VS3 coils have negligible effects, as expected;
- variations for CS/PF coils are not considered, since they are not very interesting not even in measure mode, for their effects on full CER output can be compensated.

The variations on the CER outputs due to independent shifts of the upper/lower joints from their ideal location are smaller than the above cases of coils non-idealities for the same Δx,

Table 11. Measurement performance summary of the Continuous External Rogowski.

		Relative error $r\,(2\sigma)$	Absolute error Δy	Note
CER geometric non-ideality		<0.4%	—	After poloidal field compensation. Actual value will depend on effective properties of the as-installed CER.
Calibration		<0.3%	—	
TF variations		—	2.5 kA	Actual value will depend on effective Properties of the as-installed CER.
Integrator drift		—	2.6 kA @ 3600 s	Negligible during breakdown (very beginning of pulse).
Total error	Low-range (breakdown)	<0.5 %	2.5 kA	
	Low-range (end of pulse)		3.6 kA @ 3600 s	
	High-range		3.6 kA @ 3600 s	

Δy, Δz (or of the same order of magnitude when considering the extreme cases, e.g. the output due to the PF6 current and a shift of the lower joint).

To estimate the total calibration error, the 2σ parameter corresponding to the poloidal field coils current measurement (estimated to be 0.2%) has to be considered too. In this respect, the possibility of simultaneously using several independent sources (e.g. PF3, PF4 & CS1) is helpful to reduce this effect. In case of using instead, for instance, only PF4, the corresponding error value to be added (table 10) is negligible. In conclusion, the total calibration error is estimated as being less than 0.3%, which is smaller than the specification value (0.45% [10]).

14. Noise and integration drift

The CER should not be affected by nuclear effects due to the shielding of the Vacuum Vessel. The remaining effects to be considered which generate noise are hence those due to the electronics.

As already mentioned with reference to the calibration, the 2σ parameter corresponding to the poloidal field coils current measurement is estimated to be 0.2%.

The drift of the electronic integrator is only relevant in measure mode, and not during the in-situ calibration phase, since the calibration lasts for a short period of time. The target parameter of the electronic integrator which imply integration drift is an input offset voltage of 70 μ Vs 1000^{-1} s^{-1} (2σ) [9, 13, 26–28]. Extrapolated at the ITER plasma duration (3600 s) that reads 0.25 mVs which, divided by the ideal sensitivity, M_0 (table 1), gives the maximum drift integration error of 2.6 kA (2σ).

15. Conclusions

This work provides important contributions to the state of the art of electrical current measurements by means of Rogowski sensors, in general and in particular in the nuclear fusion field, with specific reference to the ITER machine. The approximate canonical model which provides the classical expression to calculate the flux linkage is quantitatively validated. The new formula (6) generalizes the classical one and allows to evaluate the effects of the non-ideal geometry of the winding due to unavoidable imperfect manufacturing. A statistical model is proposed, which consents to compute the expected measurement error. Methods to estimate minimum and maximum error bounds due to the various types of geometrical imperfections are provided too.

The specification of the Continuous External Rogowski define the maximum measurement error 2σ in two different operating ranges (see (1)). The analyses carried out in the paper show that the specifications are met. Many causes of error have been considered, which can be classified as follows:

- irrelevant error sources:
  - approximation of the windings as sequences of planar turns: error <1 ppm;
  - presence of the joints: error negligible (small and compensable);
  - cross talk of the CS/PF/VS3 coils: it is due to the presence of the joints and to the geometrical deviation of the CER, and in measure mode can effectively be compensated;
  - non-ideal geonetric configuration of the PF3, PF4 and CS1 coils, which are then particularly suitable to perform the split calibration; also important is the fact that a survey of the as-installed CER is not needed;
  - ferromagnetic inserts: incidence of about 20 ppm;
  - nuclear effects: error negligible (the CER is shielded by the VV);
- main error sources:
  - deviation from ideal geometry of the CER windings: $2\sigma < 0.4\%$;
  - calibration (either for VS or split calibration type): $2\sigma <$ 0.3%, mostly due to the uncertainty on the poloidal field coils current measurement and less than specification (0.45%);
- sources of absolute errors, relevant at low range:
  - uncertainty due to the TF variations induced by the plasma para/dia-magnetism, conservatively estimated as $2\sigma = 2.5$ kA (relevant possibly at breakdown/ramp-up and at ramp-down);
  - integrator drift: $2\sigma_{max} = 2.6$ kA @ 3600 s (relevant at ramp-down only).

Synthetically, the digitally recorded output of the Rogowski can be expressed as:

$$y = y_0(1 + r) + \Delta y \tag{8}$$

where y_0 is the exact value of the total toroidal current being measured, r is a random variable representing the relative error of the measurement and Δy is the random absolute error, which is due to the drift of the integrator and to TF variations. Table 11 provides the quantitative details of the relevant error sources and of the total measurement error as two times the standard deviation.

Acknowledgments

The authors warmly wish to thank E. Strait, B. Xiao, A. Werner and T. Todd for their particularly active participation to the design review activities of the CER diagnostic for the parts relevant to the content of the paper. Doctors Xiao, Werner and Todd highlighted the importance of performing a thorough assessment of, respectively, the performances at low plasma current, the centricity effect and the toroidal field variations. Dr. Todd also had the important idea of using the split method to calibrate the diagnostic.

The authors also wish to thank G. Miano, G. Rubinacci and F. Villone for their active support, and G. Ambrosino, V. Coccorese, G. Lupò, C. Petrarca, G. De Tommasi, A. Formisano, R. Martone, M. Mattei, P. Moreau, S. Peruzzo and C. Serpico for fruitful discussions and useful suggestions.

This work was partly funded by F4E under grant F4E/GRT047, by the DIETI Department of Università Federico II under fund 000010-PRD-2016-G-MIANO_001_00 Elettromagnetismo Applicato and supported by the Italian MIUR under PRIN grant 2010SPS9B3. The views and opinions expressed herein do not necessarily reflect those of F4E, nor those of the ITER Organization.

References

[1] Chattock A.P. 1887 On a magnetic potentiometer *Proc. Phys. Soc.* **9** 23–6
[2] Rogowski W. and Steinhaus W. 1912 Die Messung der magnetischen Spannung *Arch. Elektrotech.* **1** 141–50
[3] Rogowski W. 1913 An improved apparatus for measuring the magnetic potential between any two points of a magnetic circuit *GB Patent* 18103
[4] Wesson J. 2004 *Tokamaks* 3rd edn (Oxford: Clarendon)
[5] Tumanski S. 2007 Induction coil sensors—a review *Meas. Sci. Technol.* **18** R31–46
[6] Quercia A. 2013 Flux linkage in helical windings and application to pick–up coils *IEEE Trans. Magn.* **49** 5692–7
[7] Quercia A. 2012 private communication
[8] Vayakis G. *et al* 2012 Development of the ITER magnetic diagnostic set and specification *Rev. Sci. Instrum.* **83** 10D712
[9] Vayakis G. 2015 System Design Description (DDD) 55.A0 Magnetic Diagnostics, v. 4.9, 14 Sep 2015 private communication
[10] Vayakis G. 2014 System Design Description (DDD) 55.A1 CER, v. 3.0, 20 Mar 2014 private communication
[11] Snipes J.A. *et al* 2014 Physics of the conceptual design of the ITER plasma control system *Fusion Eng. Des.* **89** 507–11
[12] Morimoto M.K., Ioki A., Terasawa A., Utin Y., Barabash V. and Gribov Y. 2009 Electromagnetic analysis, structural integrity, progress on mechanical design of the ITER ferromagnetic insert *Fusion Eng. Des.* **84** 2118–23
[13] Quercia A. 2013 Final report on the estimation errors on total toroidal current, Consorzio CREATE, Napoli, Italy, *Technical Report* European joint undertaking for ITER and the development of fusion energy, grant 047
[14] Olver F.W.J., Lozier D.W., Boisvert R.F. and Clark C.W. 2010 *NIST Handbook of Mathematical Functions* (Cambridge: Cambridge University Press)
[15] Moreau P. *et al* 2015 Development of the ITER Continuous External Rogowski: from conceptual design to final design *Fusion Eng. Des.* **96–7** 878–81
[16] Gribov Y. *et al* 2015 Plasma vertical stabilisation in ITER *Nucl. Fusion* **55** 073021
[17] Struik D.J. 1998 *Lectures on Classical Differential Geometry* 2nd edn (New York: Dover)
[18] Moreau P. *et al* 2013 Prototyping, testing of the Continuous External Rogowski ITER magnetic sensor *Fusion Eng. Des.* **88** 1165–9
[19] Albanese R., Hantila F.I. and Rubinacci G. 1996 A nonlinear eddy current integral formulation in terms of a two-component density vector potential *IEEE Trans. Magn.* **32** 784
[20] Albanese R. and Rubinacci G. 1998 Finite element method for the solution of 3D eddy current problems, *Adv. Images Electron Phys.* **102** 1
[21] Fresa R., Rubinacci G. and Ventre S. 2005 An eddy current integral formulation on parallel computer systems *Int. J. Numer. Methods Eng.* **62** 1127–47
[22] Albanese R. *et al* 2006 Vertical stabilization of ITER plasmas (ZCONT), Final Report on EFDA Study Contract 05–1306 (TW5-TPO-ZCONT, Milestone M2, Deliverable D2) private communication
[23] Quercia A. and Fresa R. 2012 Ex-vessel magnetic measurements in JET: a critical assessment of the collar probe *Fusion Sci. Tech.* **61** 257–74
[24] Quercia A. 2013 Final Design review of ITER Continuous External Rogowski: Measurement Performance Estimation, Chits, Commissioning Procedure *European Joint Undertaking for ITER and the Development of Fusion Energy (Barcelona, Spain, 30–31 July 2013)*
[25] Fresa R. *et al* 2015 Sensitivity of the diamagnetic sensor measurements of ITER to error sources and their compensation *Fusion Eng. Des.* **100** 133–41
[26] Bak J.G., Lee S.G. and Son D. 2004 Performance of the magnetic sensor, the integrator for the KSTAR magnetic diagnostics *Rev. Sci. Instrum.* **75** 4305–7
[27] Bak J.G., Lee S.G., Son D. and Ga E.M. 2007 Analog integrator for the Korea superconducting tokamak advanced research magnetic diagnostics *Rev. Sci. Instrum.* **78** 043504
[28] Carvalho B.B., Batista A., Zilker M., Rahbarnia K. and The W7-X CoDaC Team 2017 Design, implementation and commissioning of ATCA based high-speed multichannel data acquisition systems for magnetic diagnostics in W7-X *11th IAEA Technical Meeting on Control, Data Acquisition and Remote Participation for Fusion Research (Greifswald, Germany, 08–12 May 2017)*